Supplement of Geosci. Model Dev., 17, 2901–2927, 2024
https://doi.org/10.5194/gmd-17-2901-2024-supplement

Geoscientific Model Development
Open Access
EGU

Supplement of

Challenges of constructing and selecting the "perfect" boundary conditions for the large-eddy simulation model PALM

Jelena Radović et al.

Correspondence to: Jelena Radović (jelena.radovic@matfyz.cuni.cz)

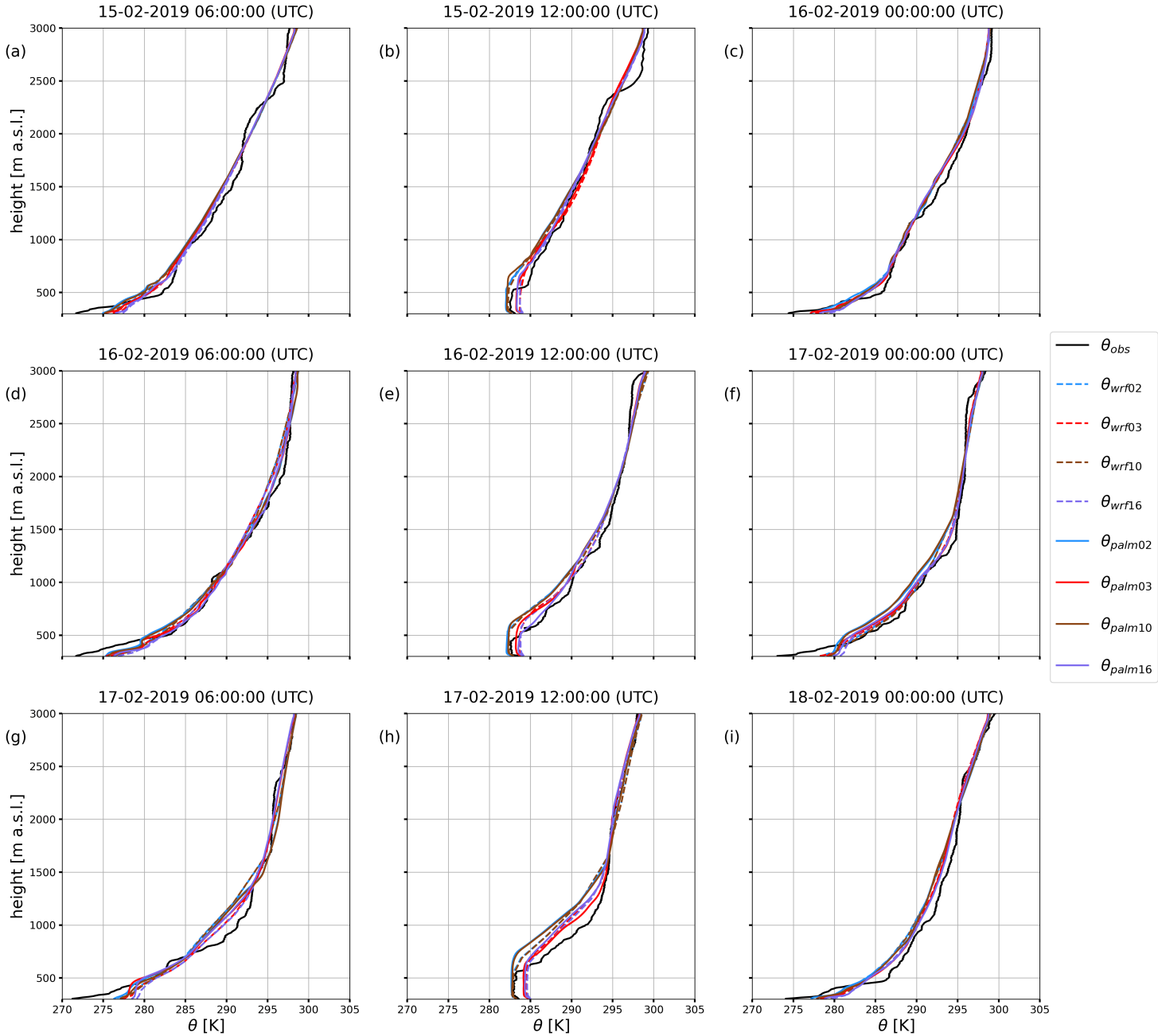

Figure S01: Vertical profiles of potential temperature from the radio sounding observations at Praha-Libuš station (WMO ID 11520; solid black line), selected members of the WRF model ensemble (taken at the grid box closest to the observation station; colored dashed lines), and the PALM model simulations (averaged over the 10 x 10 grid box area around the center of the domain; colored solid lines) for the e1 episode up to the height of 3000 m a.s.l.

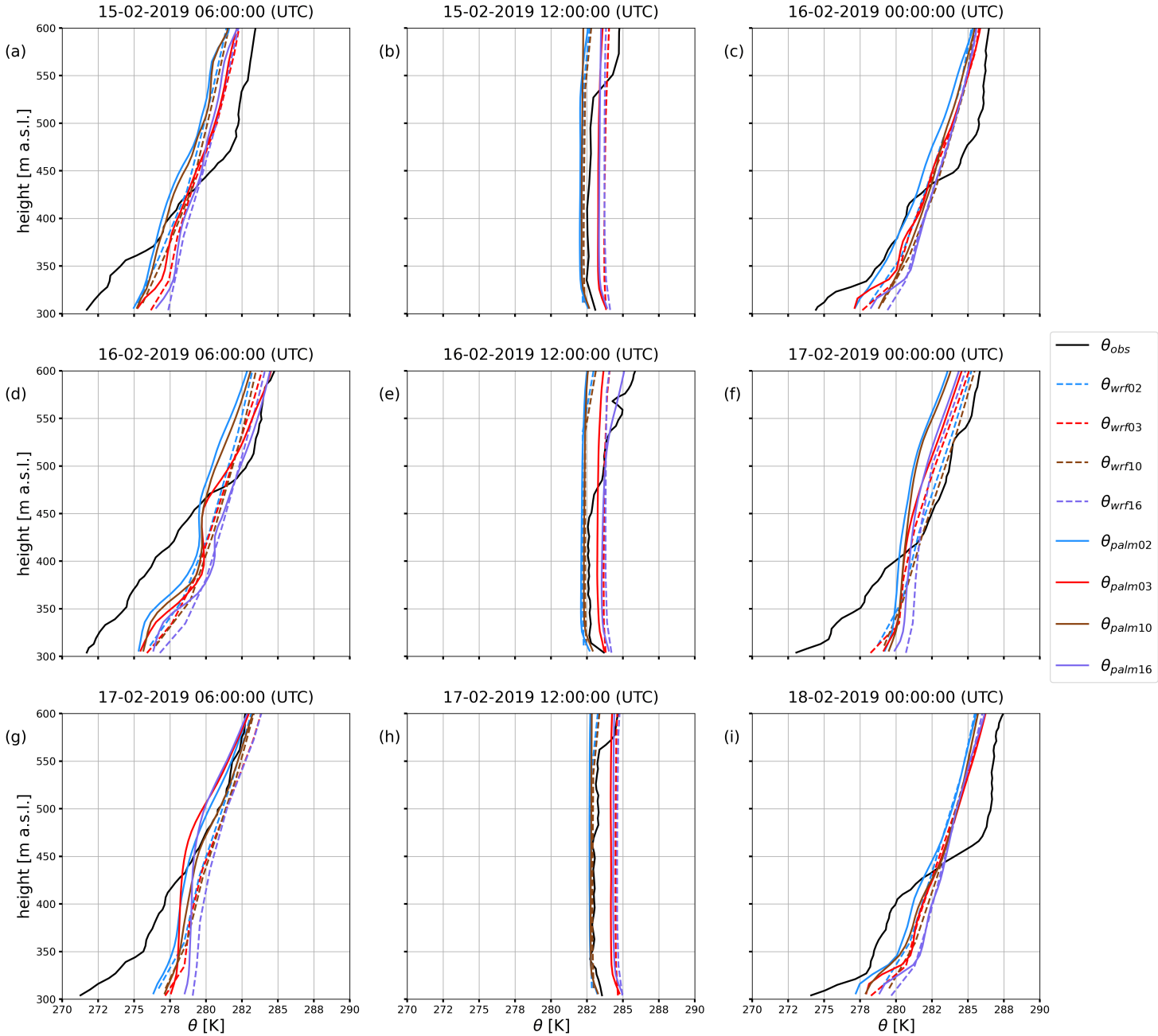

Figure S02: Vertical profiles of potential temperature from the radio sounding observations at Praha-Libuš station (WMO ID 11520; solid black line), selected members of the WRF model ensemble (taken at the grid box closest to the observation station; colored dashed lines), and the PALM model simulations (averaged over the 10 x 10 grid box area around the center of the domain; colored solid lines) for the e1 episode up to the height of 600 m a.s.l.

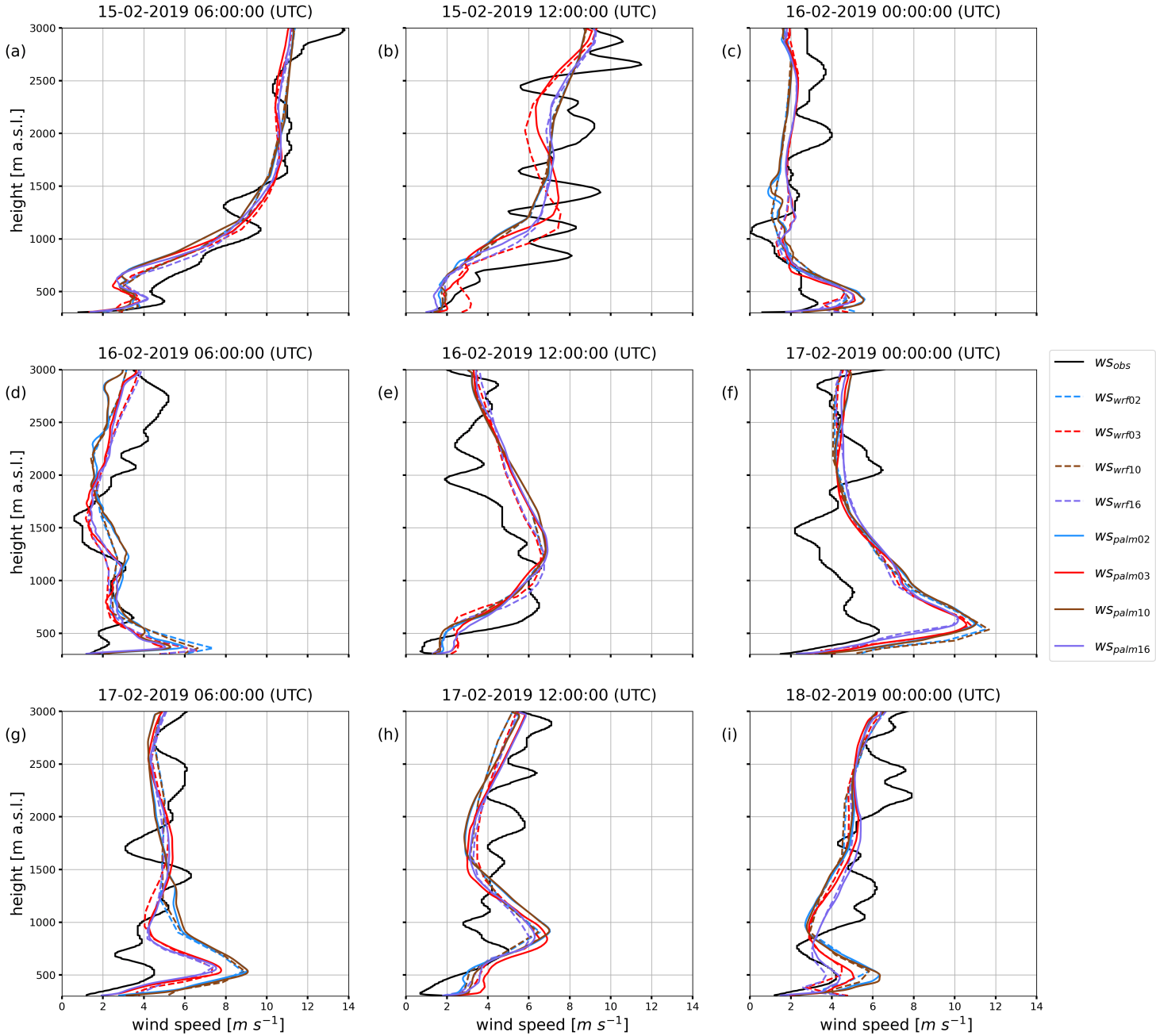

Figure S03: Vertical profiles of wind speed from the radio sounding observations at Praha-Libuš station (WMO ID 11520; solid black line), selected members of the WRF model ensemble (taken at the grid box closest to the observation station; colored dashed lines), and the PALM model simulations (averaged over the 10 x 10 grid box area around the center of the domain; colored solid lines) for the e1 episode up to the height of 3000 m a.s.l.

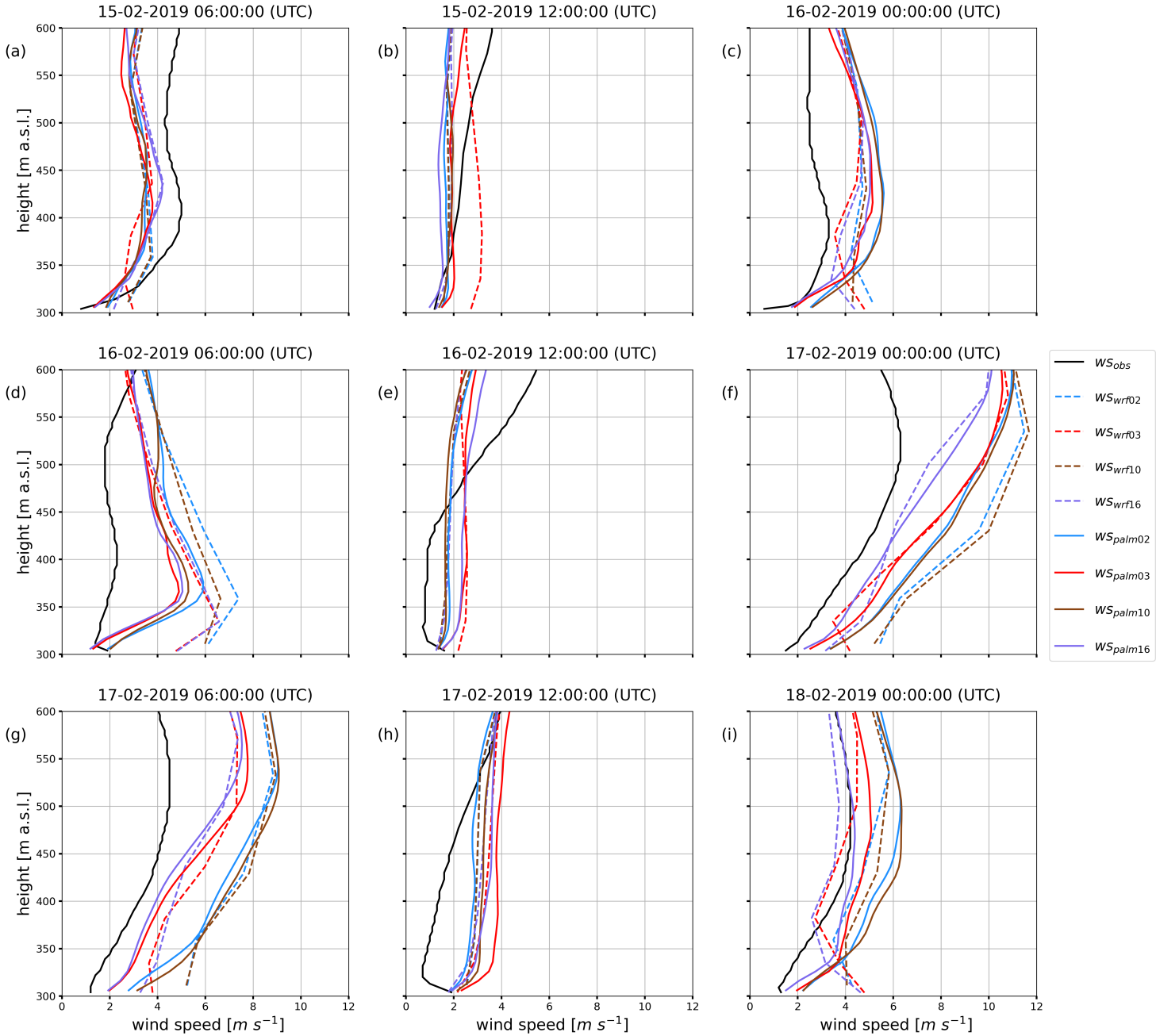

Figure S04: Vertical profiles of wind speed from the radio sounding observations at Praha-Libuš station (WMO ID 11520; solid black line), selected members of the WRF model ensemble (taken at the grid box closest to the observation station; colored dashed lines), and the PALM model simulations (averaged over the 10 x 10 grid box area around the center of the domain; colored solid lines) for the e1 episode up to the height of 600 m a.s.l.

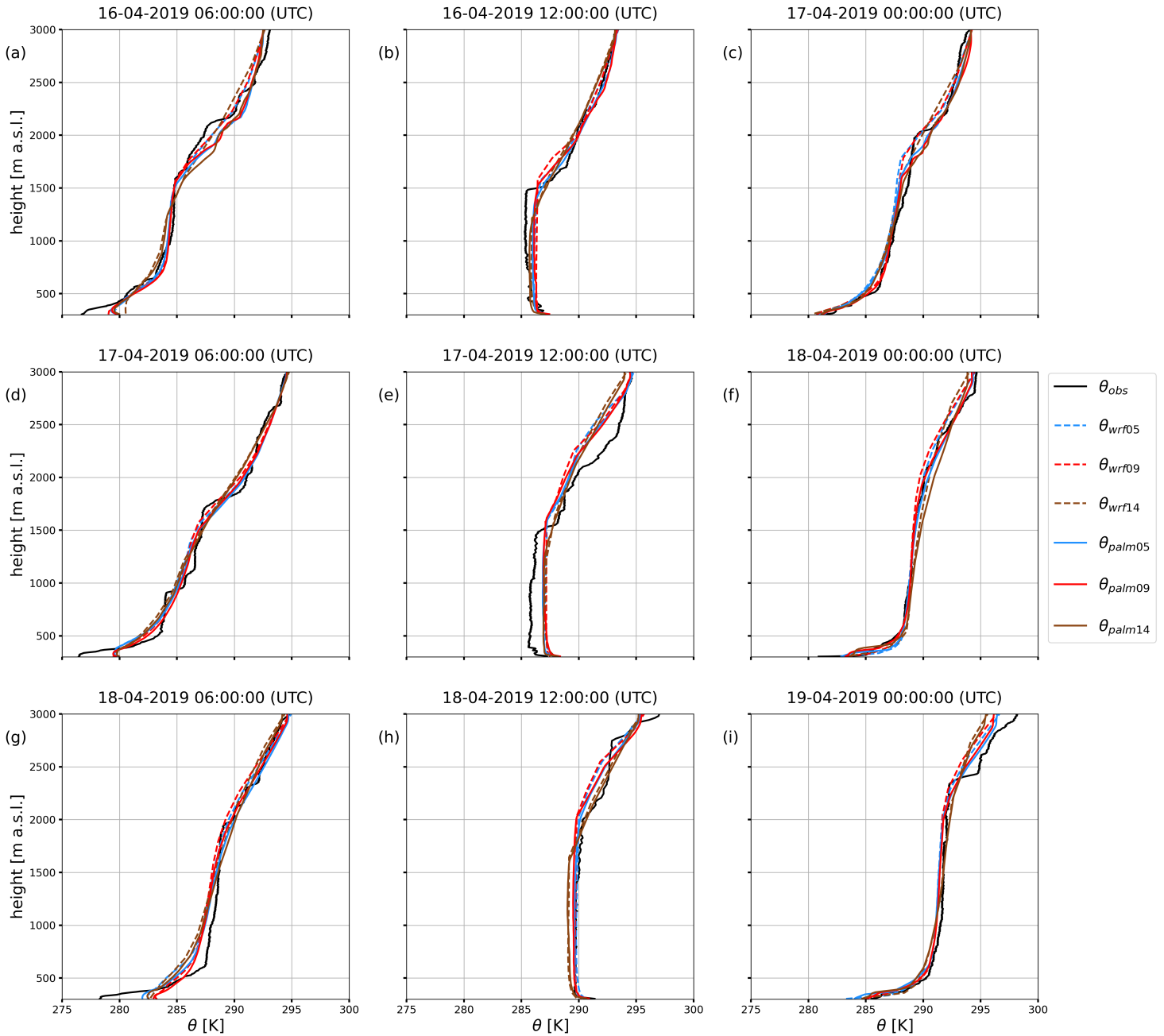

Figure S05: Vertical profiles of potential temperature from the radio sounding observations at Praha-Libuš station (WMO ID 11520; solid black line), selected members of the WRF model ensemble (taken at the grid box closest to the observation station; colored dashed lines), and the PALM model simulations (averaged over the 10 x 10 grid box area around the center of the domain; colored solid lines) for the e2 episode up to the height of 3000 m a.s.l.

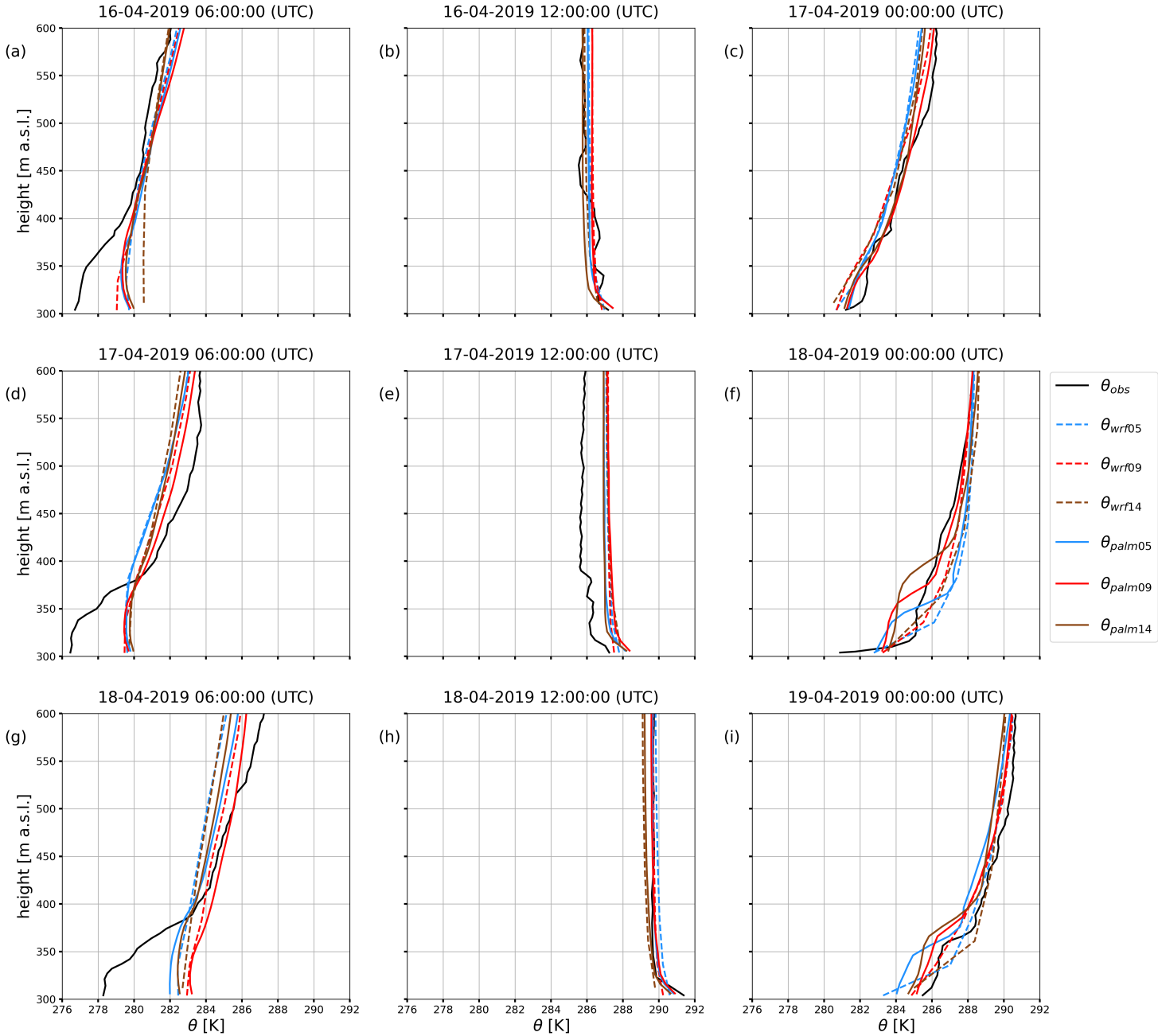

Figure S06: Vertical profiles of potential temperature from the radio sounding observations at Praha-Libuš station (WMO ID 11520; solid black line), selected members of the WRF model ensemble (taken at the grid box closest to the observation station; colored dashed lines), and the PALM model simulations (averaged over the 10 x 10 grid box area around the center of the domain; colored solid lines) for the e2 episode up to the height of 600 m a.s.l.

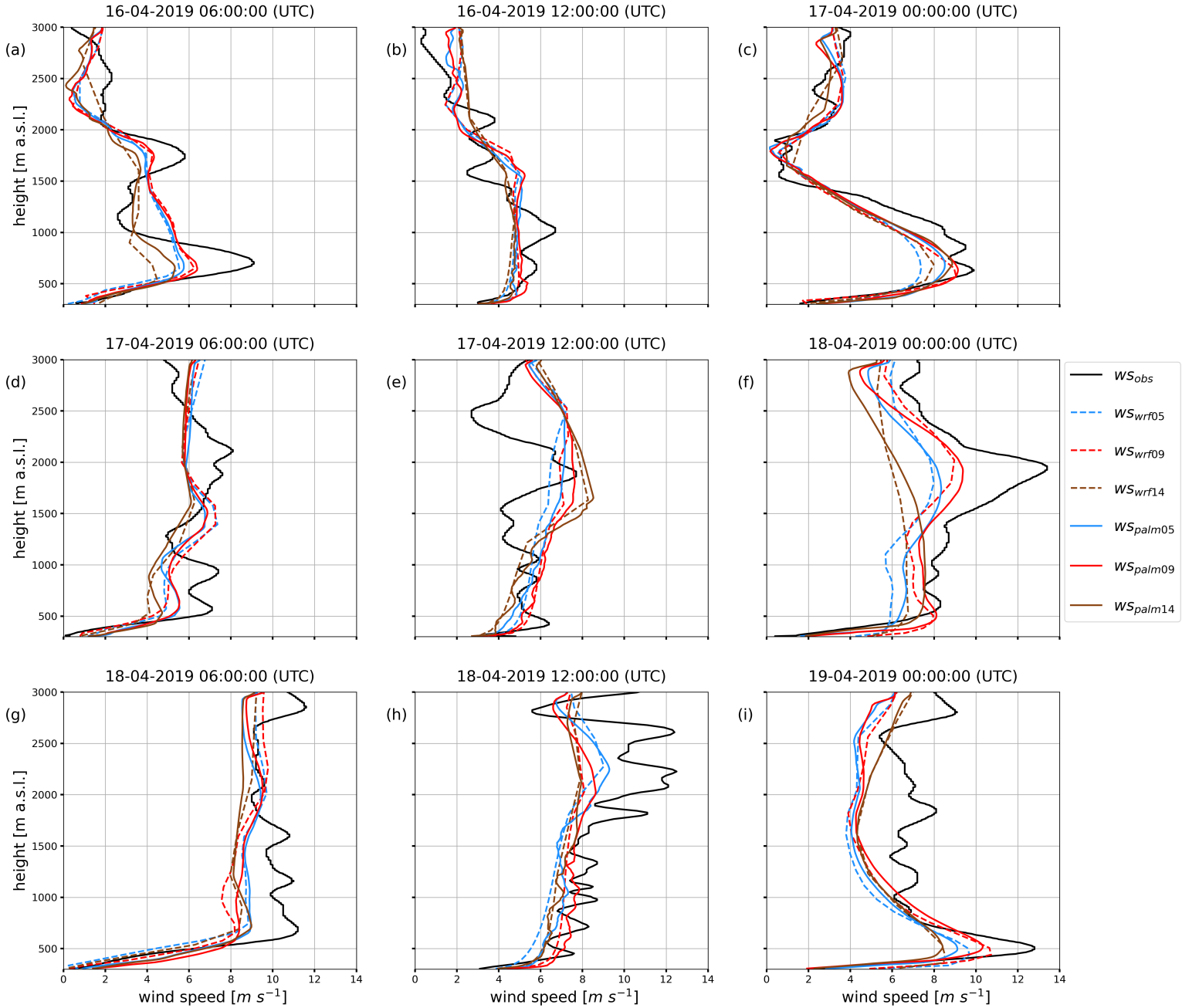

Figure S07: Vertical profiles of wind speed from the radio sounding observations at Praha-Libuš station (WMO ID 11520; solid black line), selected members of the WRF model ensemble (taken at the grid box closest to the observation station; colored dashed lines), and the PALM model simulations (averaged over the 10 x 10 grid box area around the center of the domain; colored solid lines) for the e2 episode up to the height of 3000 m a.s.l.

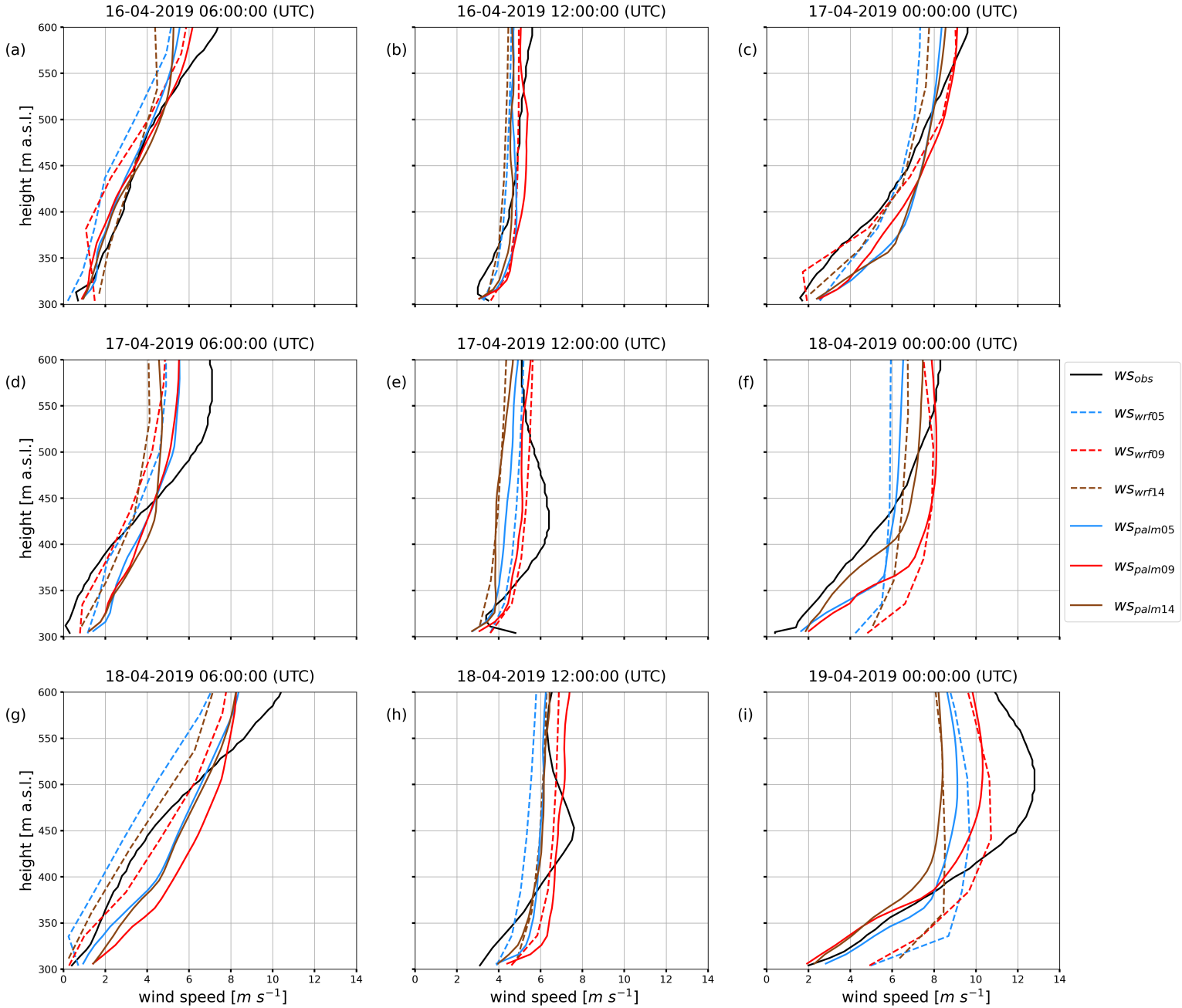

Figure S08: Vertical profiles of wind speed from the radio sounding observations at Praha-Libuš station (WMO ID 11520; solid black line), selected members of the WRF model ensemble (taken at the grid box closest to the observation station; colored dashed lines), and the PALM model simulations (averaged over the 10 x 10 grid box area around the center of the domain; colored solid lines) for the e2 episode up to the height of 600 m a.s.l.

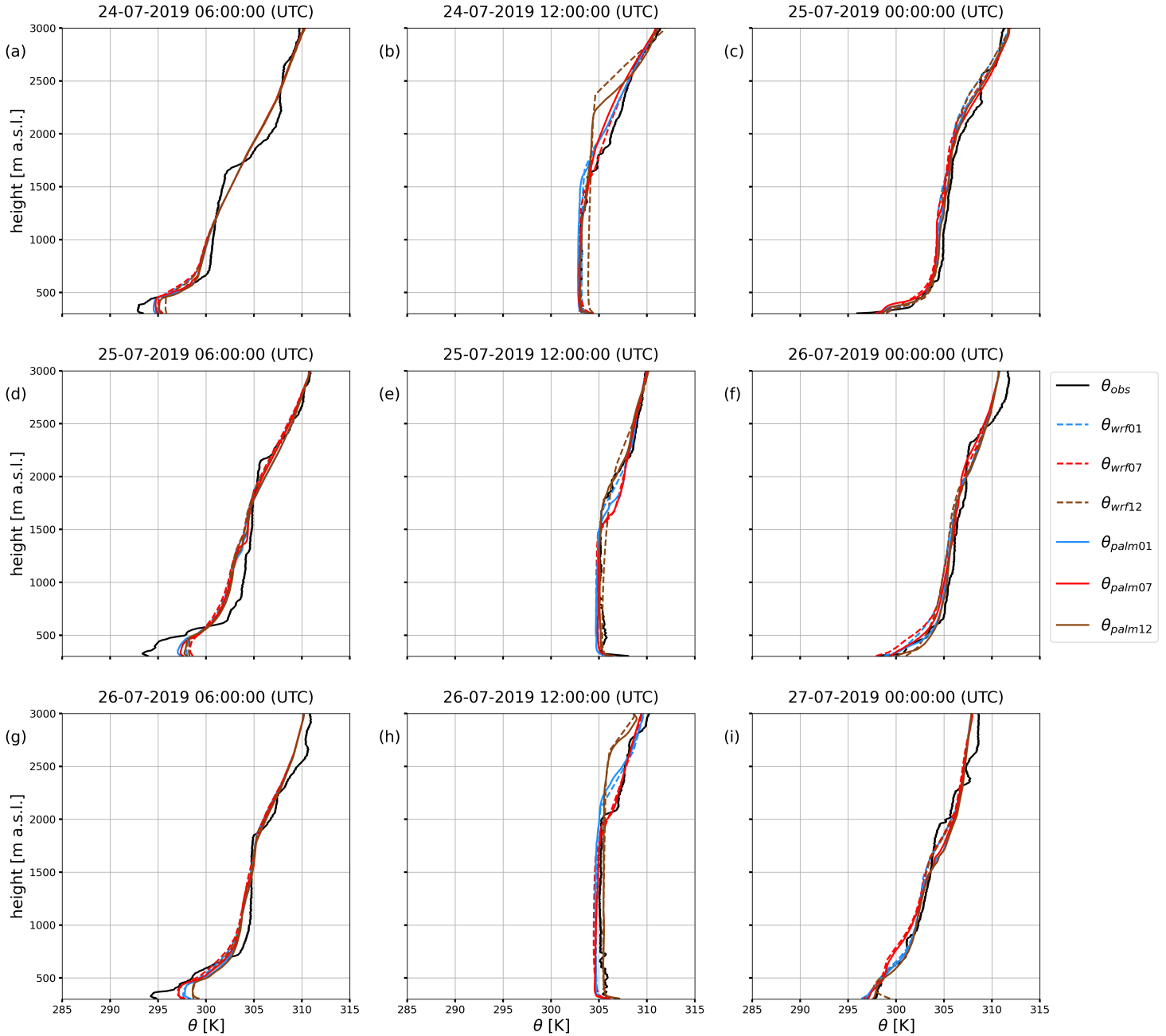

Figure S09: Vertical profiles of potential temperature from the radio sounding observations at Praha-Libuš station (WMO ID 11520; solid black line), selected members of the WRF model ensemble (taken at the grid box closest to the observation station; colored dashed lines), and the PALM model simulations (averaged over the 10 x 10 grid box area around the center of the domain; colored solid lines) for the e3 episode up to the height of 3000 m a.s.l.

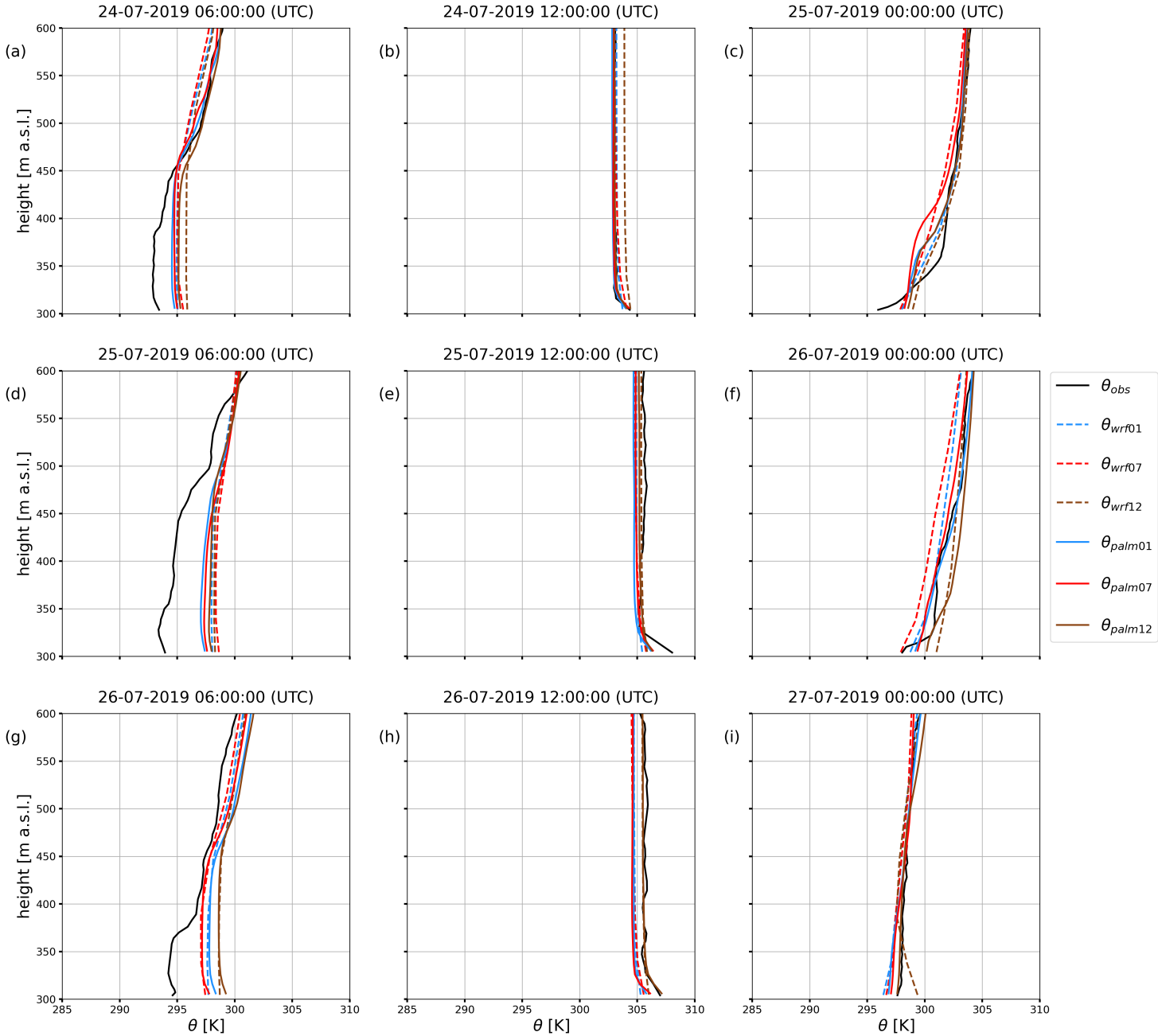

Figure S10: Vertical profiles of potential temperature from the radio sounding observations at Praha-Libuš station (WMO ID 11520; solid black line), selected members of the WRF model ensemble (taken at the grid box closest to the observation station; colored dashed lines), and the PALM model simulations (averaged over the 10 x 10 grid box area around the center of the domain; colored solid lines) for the e3 episode up to the height of 600 m a.s.l.

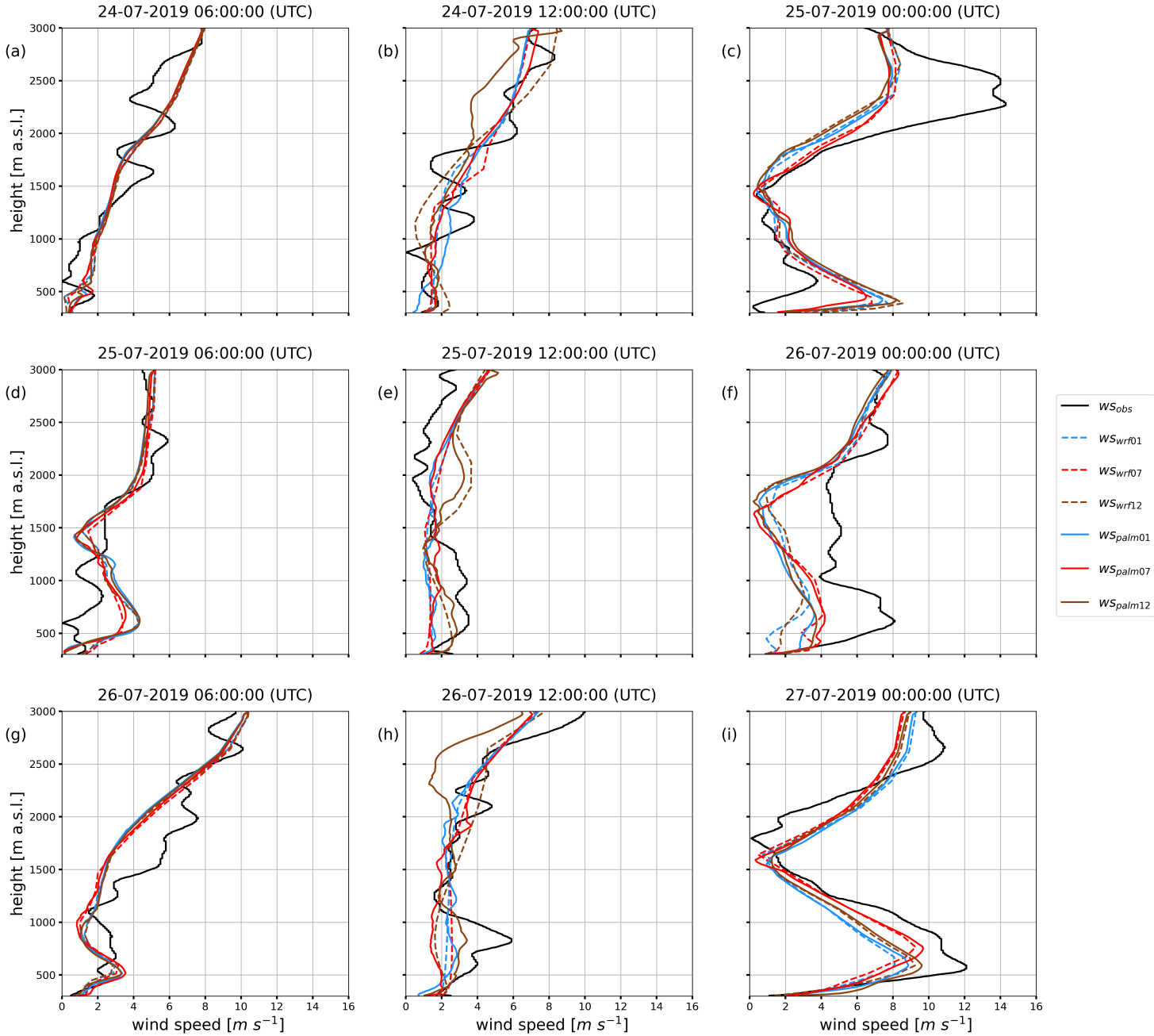

Figure S11: Vertical profiles of wind speed from the radio sounding observations at Praha-Libuš station (WMO ID 11520; solid black line), selected members of the WRF model ensemble (taken at the grid box closest to the observation station; colored dashed lines), and the PALM model simulations (averaged over the 10 x 10 grid box area around the center of the domain; colored solid lines) for the e3 episode up to the height of 3000 m a.s.l.

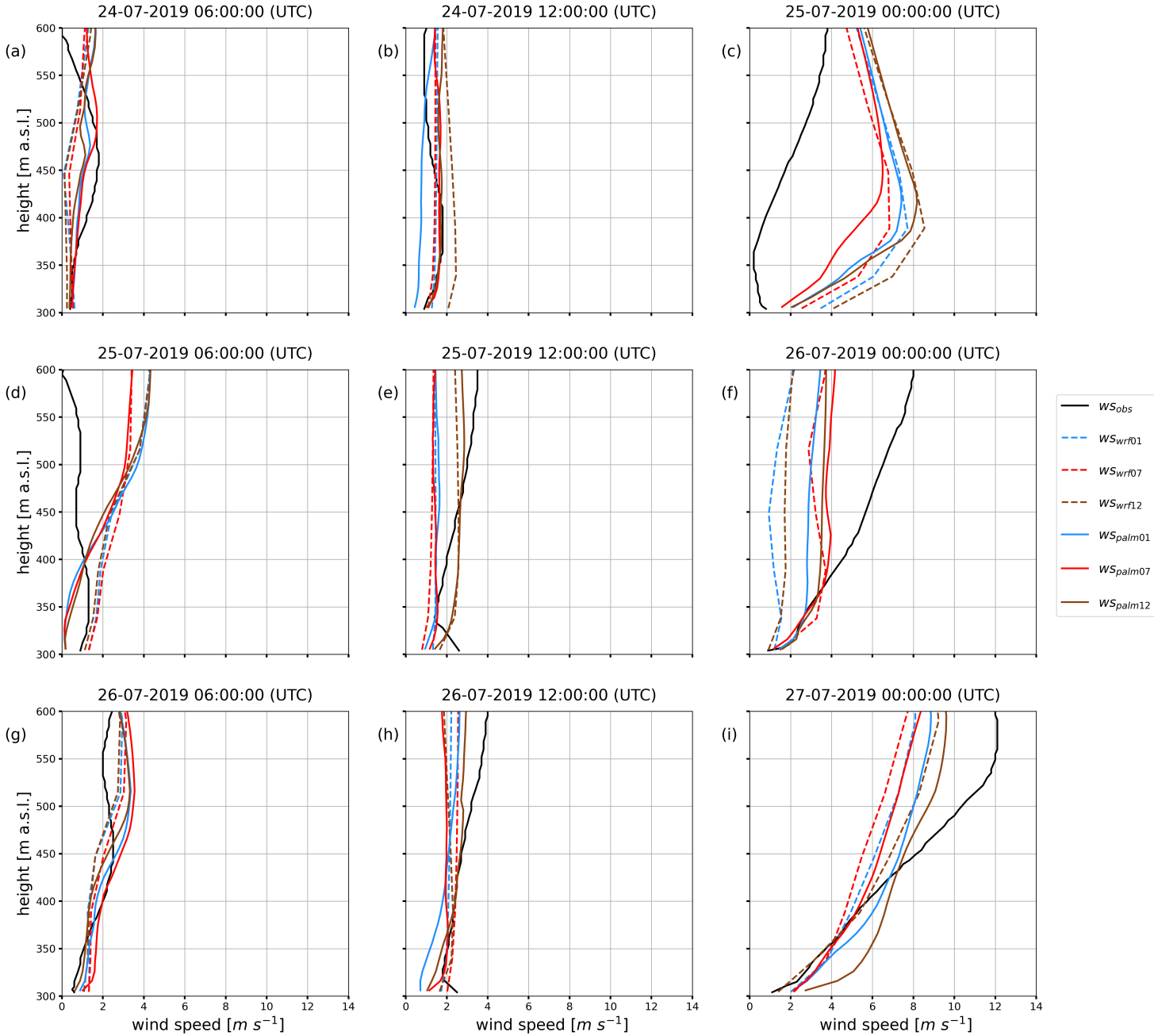

Figure S12: Vertical profiles of wind speed from the radio sounding observations at Praha-Libuš station (WMO ID 11520; solid black line), selected members of the WRF model ensemble (taken at the grid box closest to the observation station; colored dashed lines), and the PALM model simulations (averaged over the 10 x 10 grid box area around the center of the domain; colored solid lines) for the e3 episode up to the height of 600 m a.s.l.

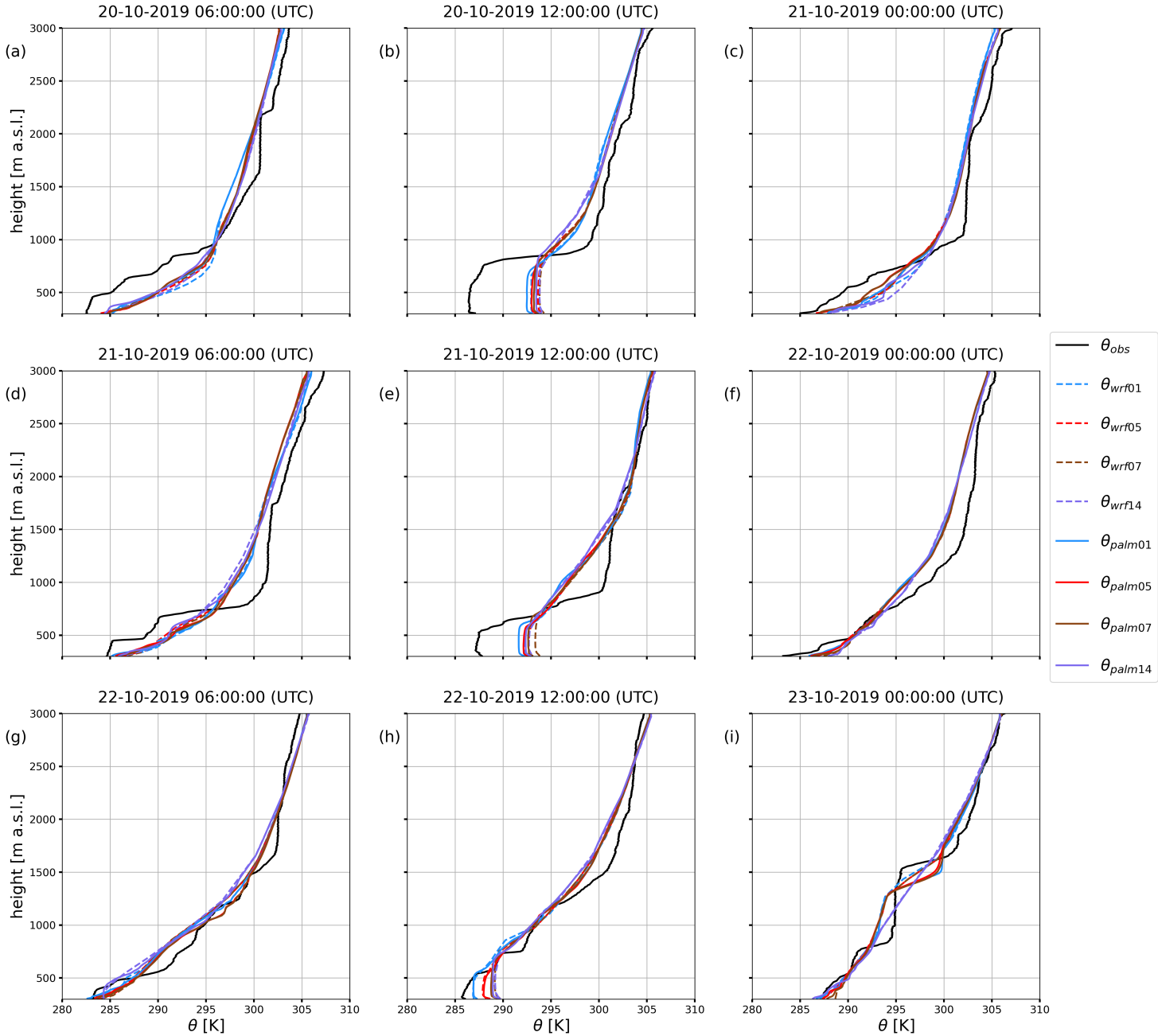

Figure S13: Vertical profiles of potential temperature from the radio sounding observations at Praha-Libuš station (WMO ID 11520; solid black line), selected members of the WRF model ensemble (taken at the grid box closest to the observation station; colored dashed lines), and the PALM model simulations (averaged over the 10 x 10 grid box area around the center of the domain; colored solid lines) for the e4 episode up to the height of 3000 m a.s.l.

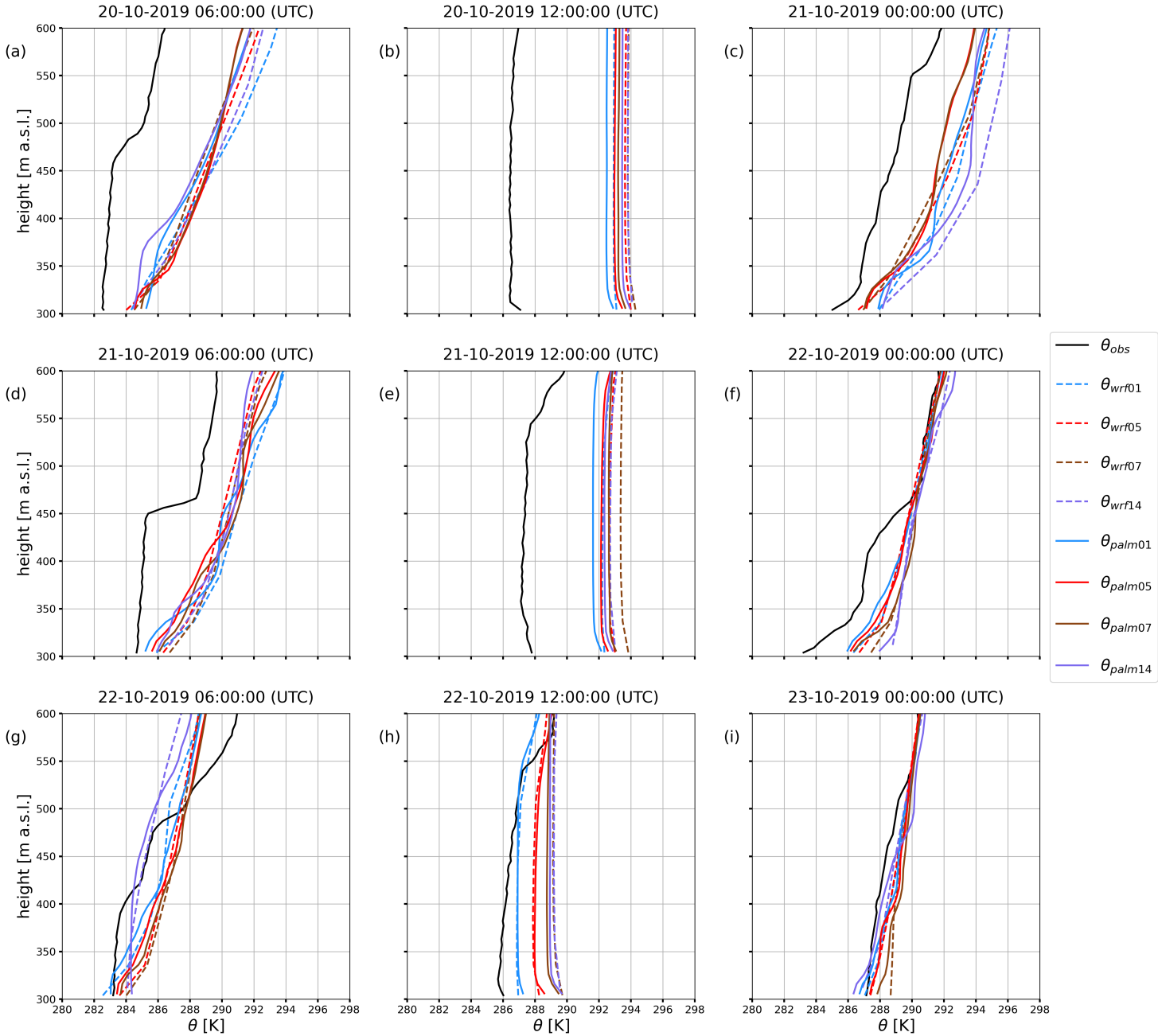

Figure S14: Vertical profiles of potential temperature from the radio sounding observations at Praha-Libuš station (WMO ID 11520; solid black line), selected members of the WRF model ensemble (taken at the grid box closest to the observation station; colored dashed lines), and the PALM model simulations (averaged over the 10 x 10 grid box area around the center of the domain; colored solid lines) for the e4 episode up to the height of 600 m a.s.l.

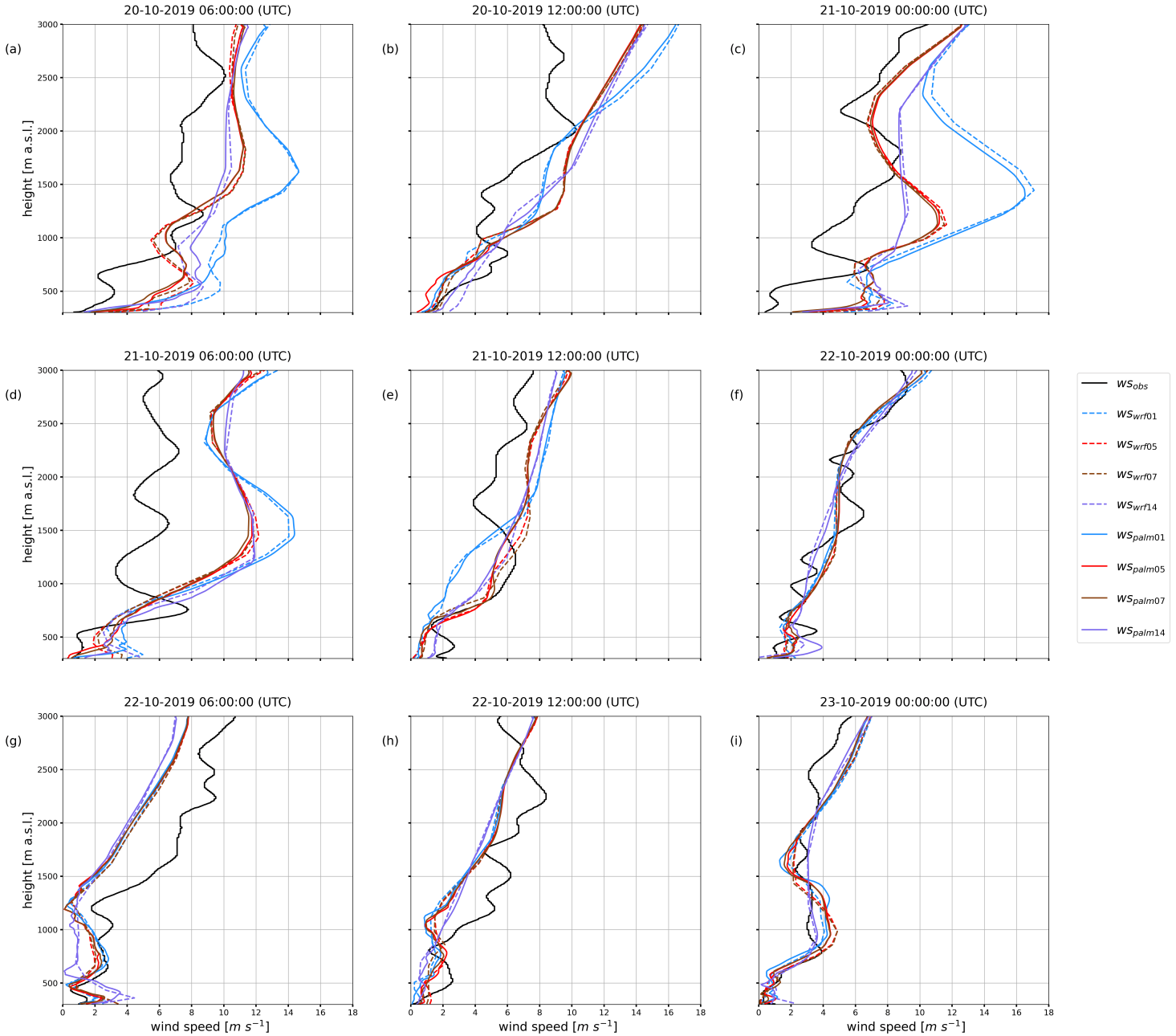

Figure S15: Vertical profiles of wind speed from the radio sounding observations at Praha-Libuš station (WMO ID 11520; solid black line), selected members of the WRF model ensemble (taken at the grid box closest to the observation station; colored dashed lines), and the PALM model simulations (averaged over the 10 x 10 grid box area around the center of the domain; colored solid lines) for the e4 episode up to the height of 3000 m a.s.l.

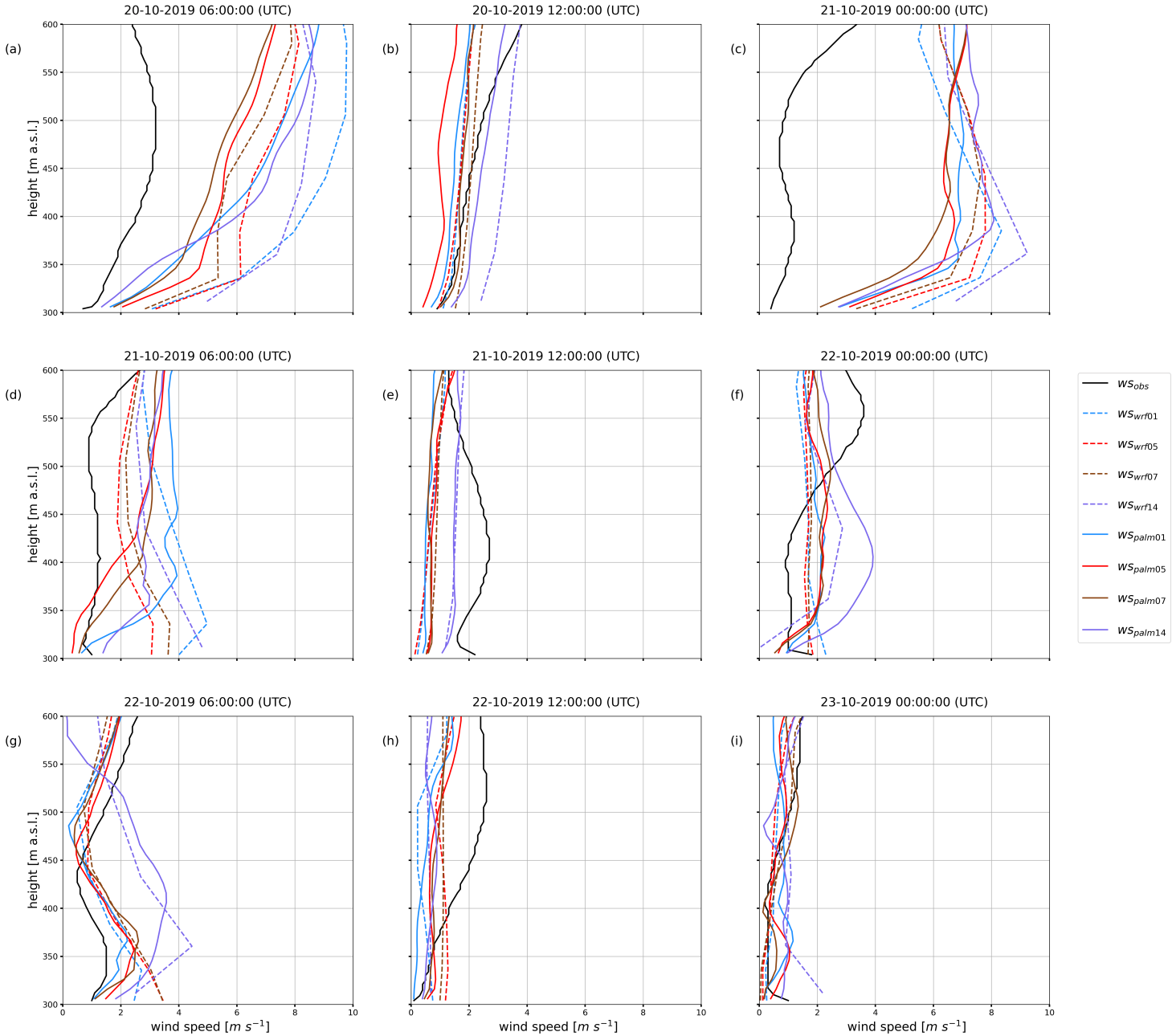

Figure S16: Vertical profiles of wind speed from the radio sounding observations at Praha-Libuš station (WMO ID 11520; solid black line), selected members of the WRF model ensemble (taken at the grid box closest to the observation station; colored dashed lines), and the PALM model simulations (averaged over the 10 x 10 grid box area around the center of the domain; colored solid lines) for the e4 episode up to the height of 600 m a.s.l.

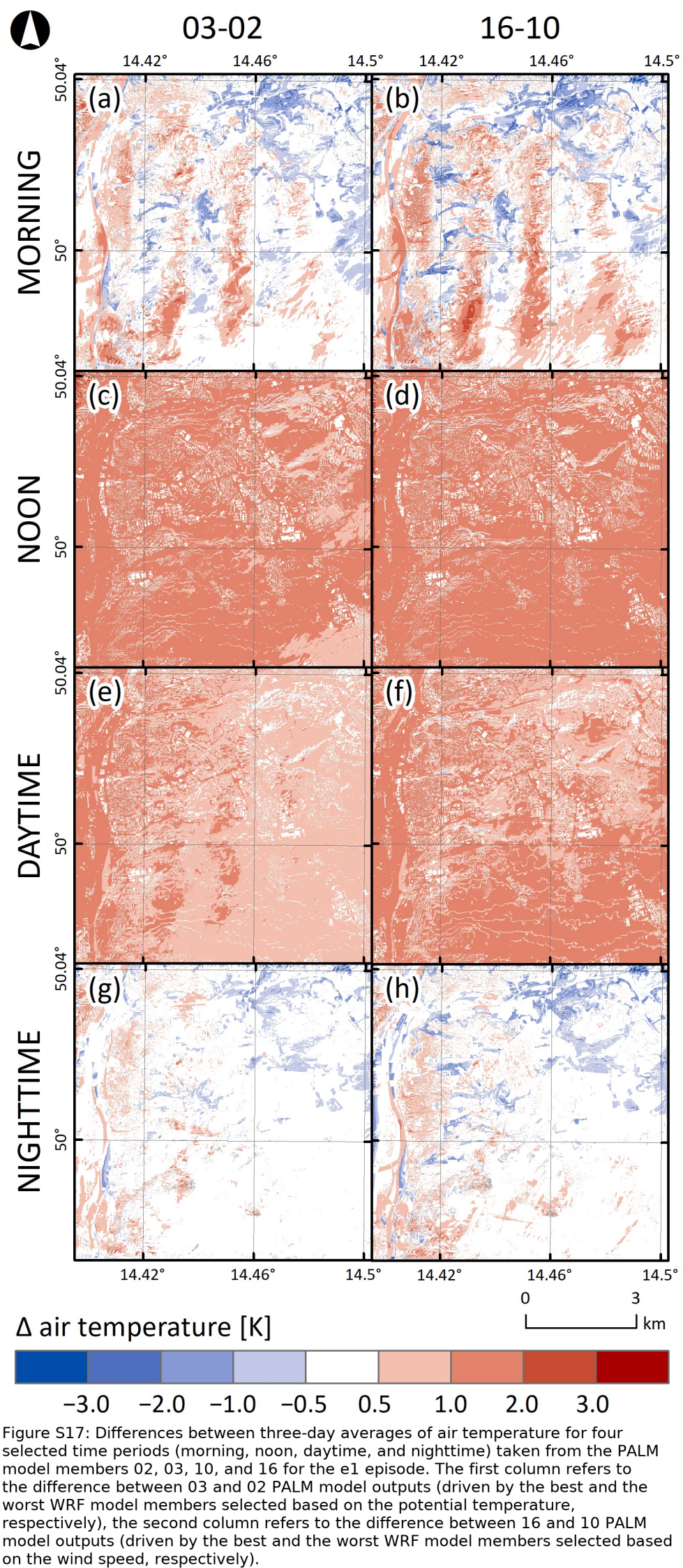

Figure S17: Differences between three-day averages of air temperature for four selected time periods (morning, noon, daytime, and nighttime) taken from the PALM model members 02, 03, 10, and 16 for the e1 episode. The first column refers to the difference between 03 and 02 PALM model outputs (driven by the best and the worst WRF model members selected based on the potential temperature, respectively), the second column refers to the difference between 16 and 10 PALM model outputs (driven by the best and the worst WRF model members selected based on the wind speed, respectively).

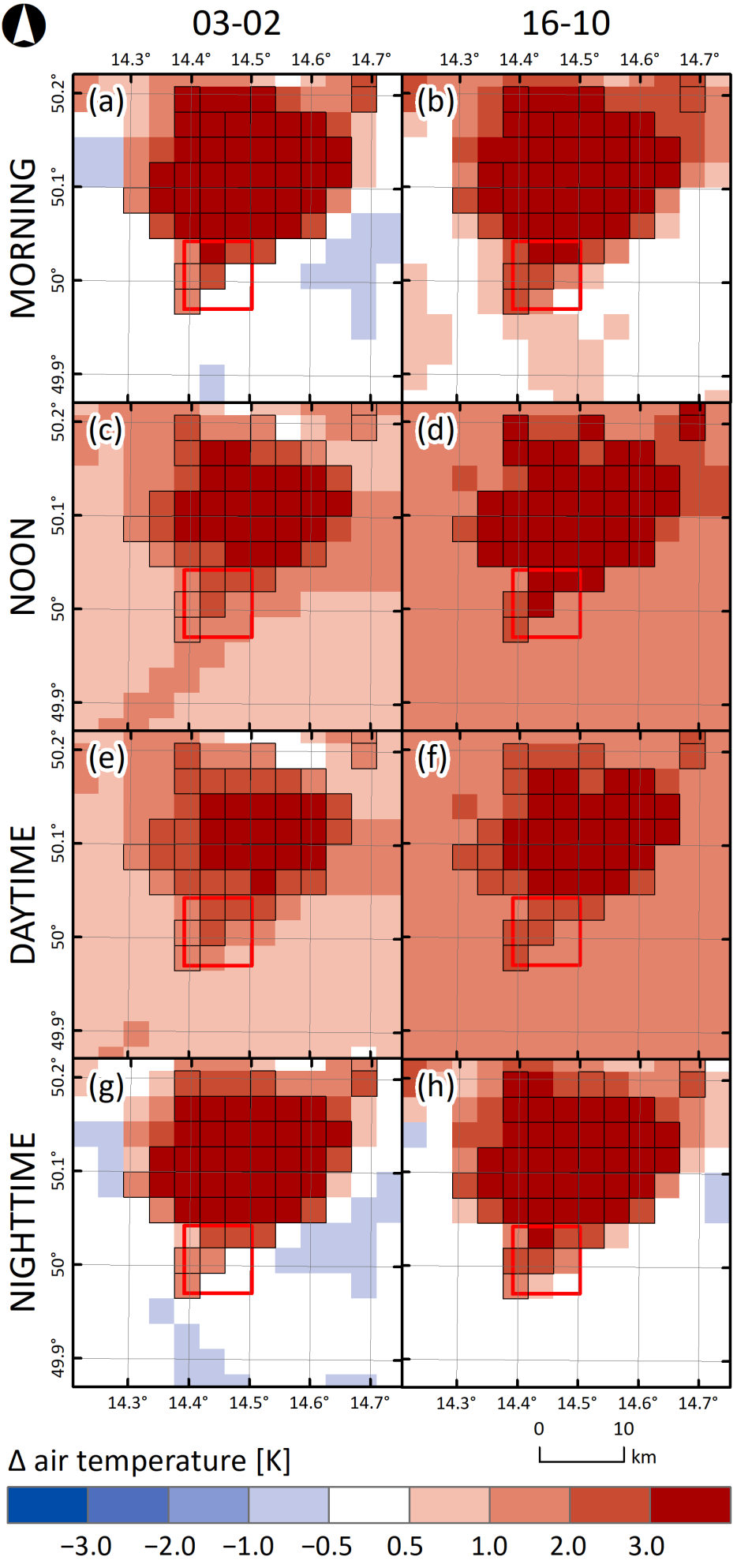

Figure S18: Differences between three-day averages of air temperature for four selected time periods (morning, noon, daytime, and nighttime) taken from the WRF model members 02, 03, 10 and 16 for the e1 episode. The first column refers to the difference between the best (03) and the worst (02) WRF model members selected based on the potential temperature, the second column refers to the difference between the best (16) and the worst (10) WRF model members selected based on the wind speed. The PALM model simulation domain is depicted with the red square. The WRF model grid boxes in which the majority of landuse is of urban type are outlined with black color.

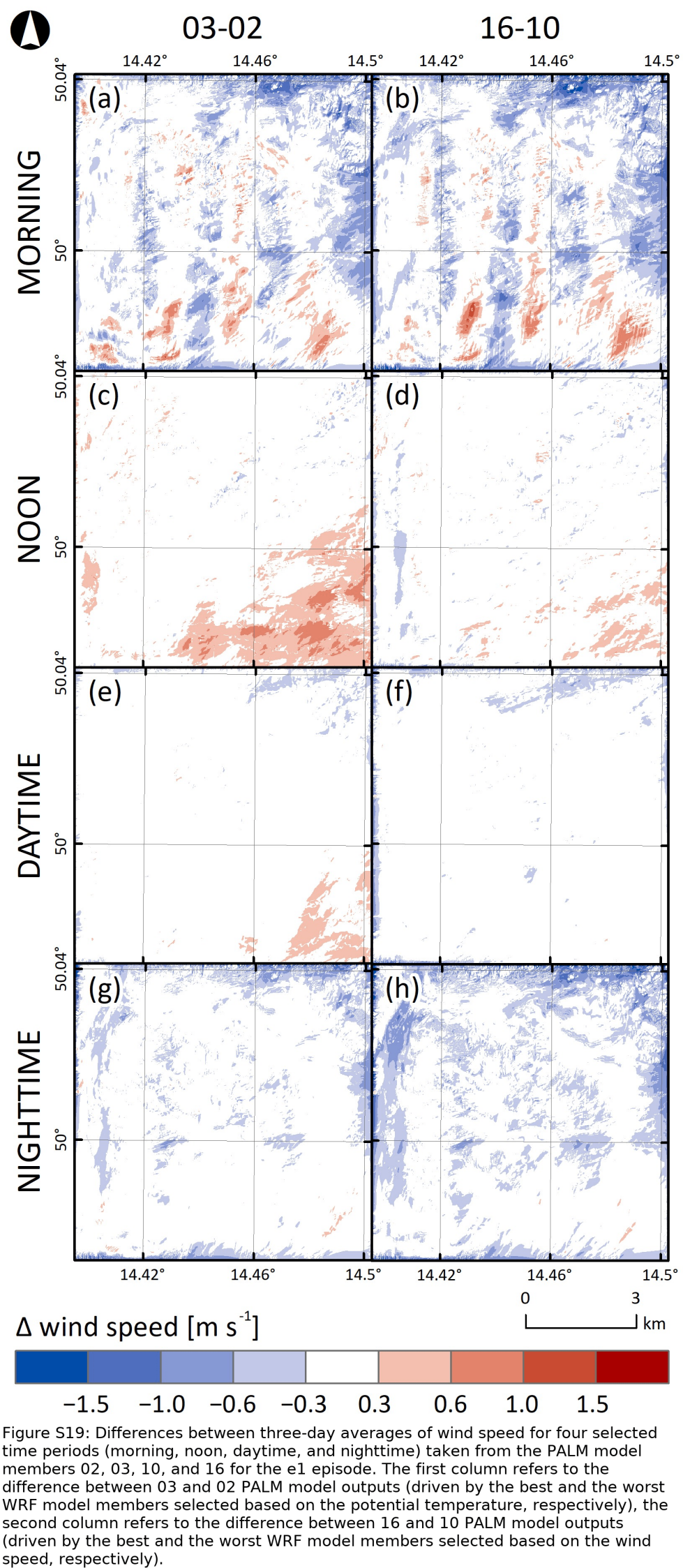

Figure S19: Differences between three-day averages of wind speed for four selected time periods (morning, noon, daytime, and nighttime) taken from the PALM model members 02, 03, 10, and 16 for the e1 episode. The first column refers to the difference between 03 and 02 PALM model outputs (driven by the best and the worst WRF model members selected based on the potential temperature, respectively), the second column refers to the difference between 16 and 10 PALM model outputs (driven by the best and the worst WRF model members selected based on the wind speed, respectively).

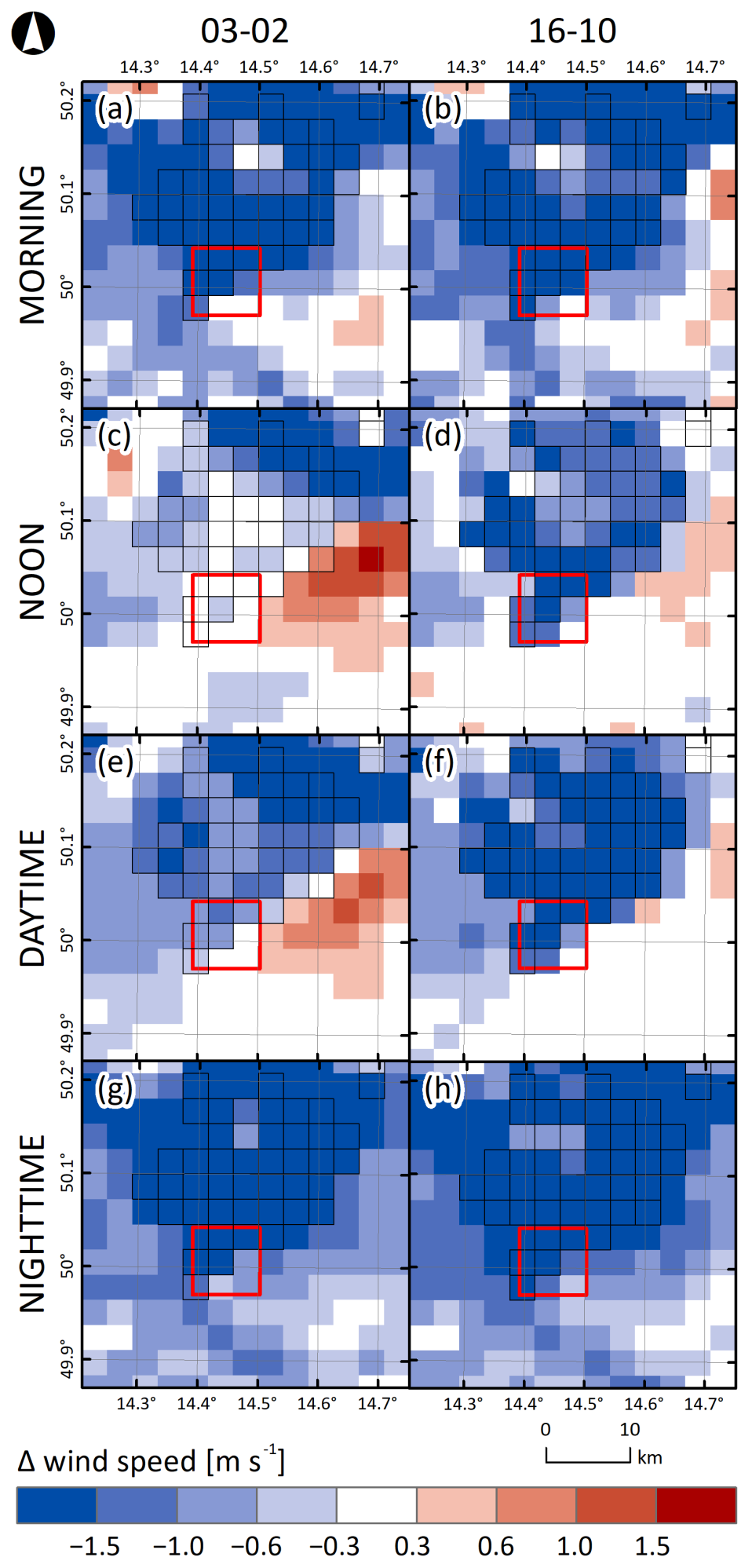

Figure S20: Differences between three-day averages of wind speed for four selected time periods (morning, noon, daytime, and nighttime) taken from the WRF model members 02, 03, 10 and 16 for the e1 episode. The first column refers to the difference between the best (03) and the worst (02) WRF model members selected based on the potential temperature, the second column refers to the difference between the best (16) and the worst (10) WRF model members selected based on the wind speed. The PALM model simulation domain is depicted with the red square. The WRF model grid boxes in which the majority of landuse is of urban type are outlined with black color.

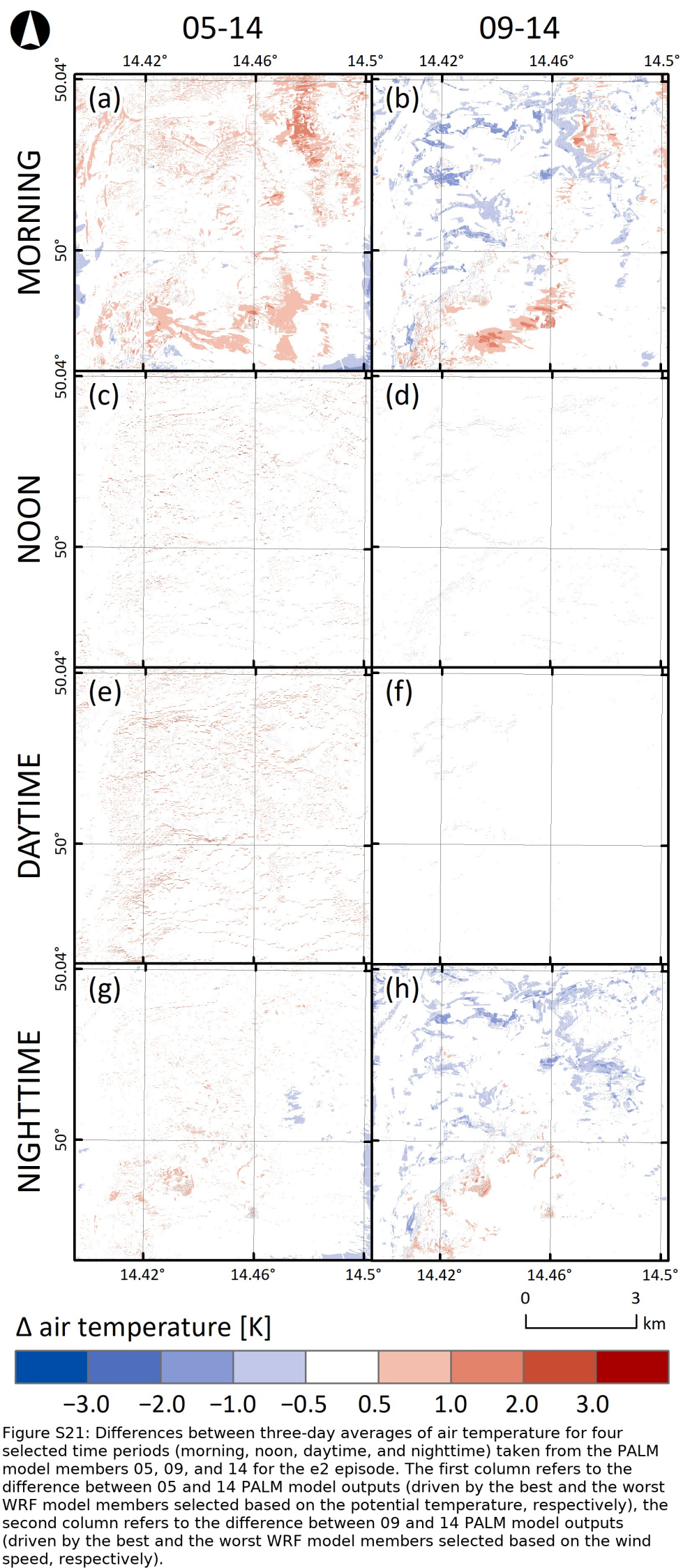

Figure S21: Differences between three-day averages of air temperature for four selected time periods (morning, noon, daytime, and nighttime) taken from the PALM model members 05, 09, and 14 for the e2 episode. The first column refers to the difference between 05 and 14 PALM model outputs (driven by the best and the worst WRF model members selected based on the potential temperature, respectively), the second column refers to the difference between 09 and 14 PALM model outputs (driven by the best and the worst WRF model members selected based on the wind speed, respectively).

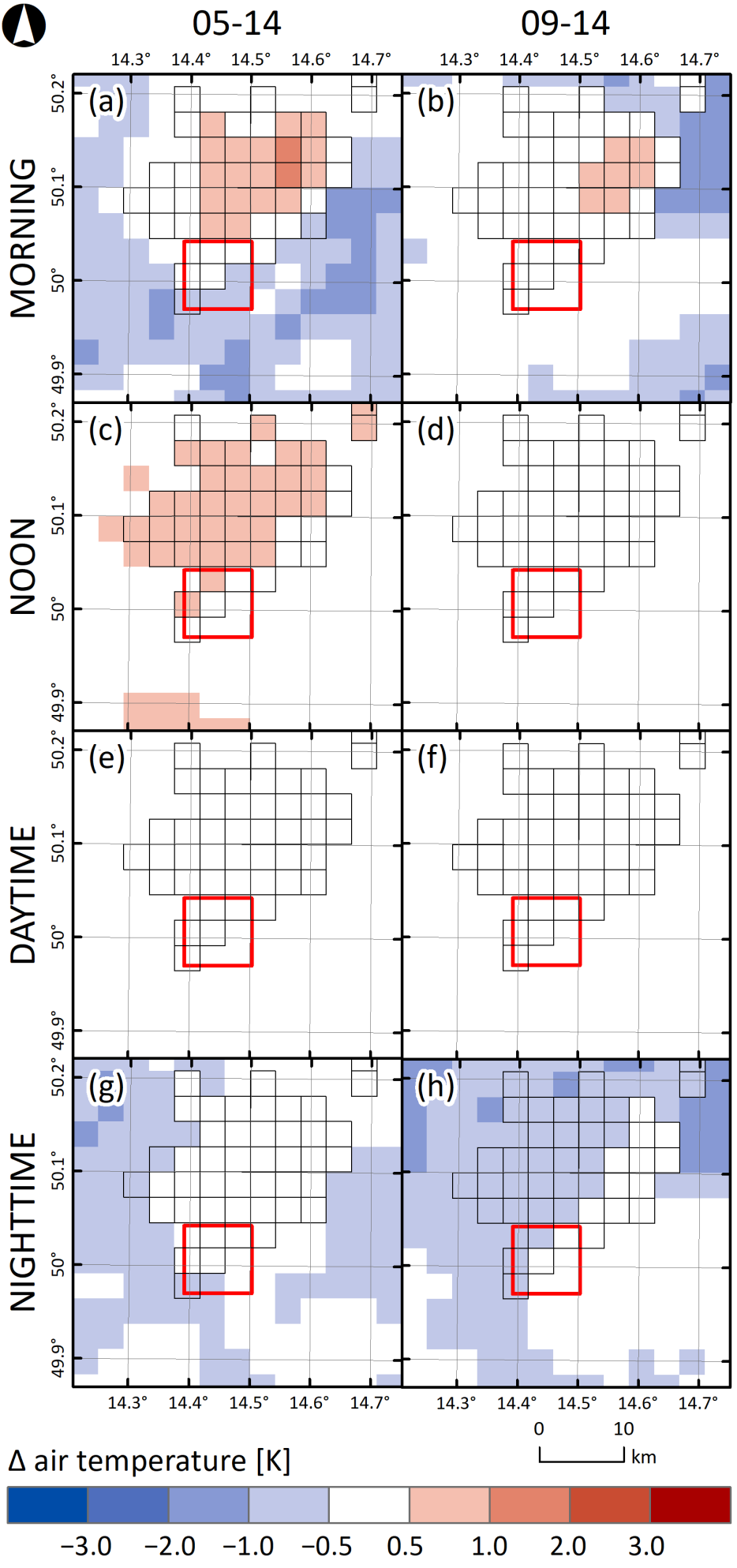

Figure S22: Differences between three-day averages of air temperature for four selected time periods (morning, noon, daytime, and nighttime) taken from the WRF model members 05, 09, and 14 for the e2 episode. The first column refers to the difference between the best (05) and the worst (14) WRF model members selected based on the potential temperature, the second column refers to the difference between the best (09) and the worst (14) WRF model members selected based on the wind speed. The PALM model simulation domain is depicted with the red square. The WRF model grid boxes in which the majority of landuse is of urban type are outlined with black color.

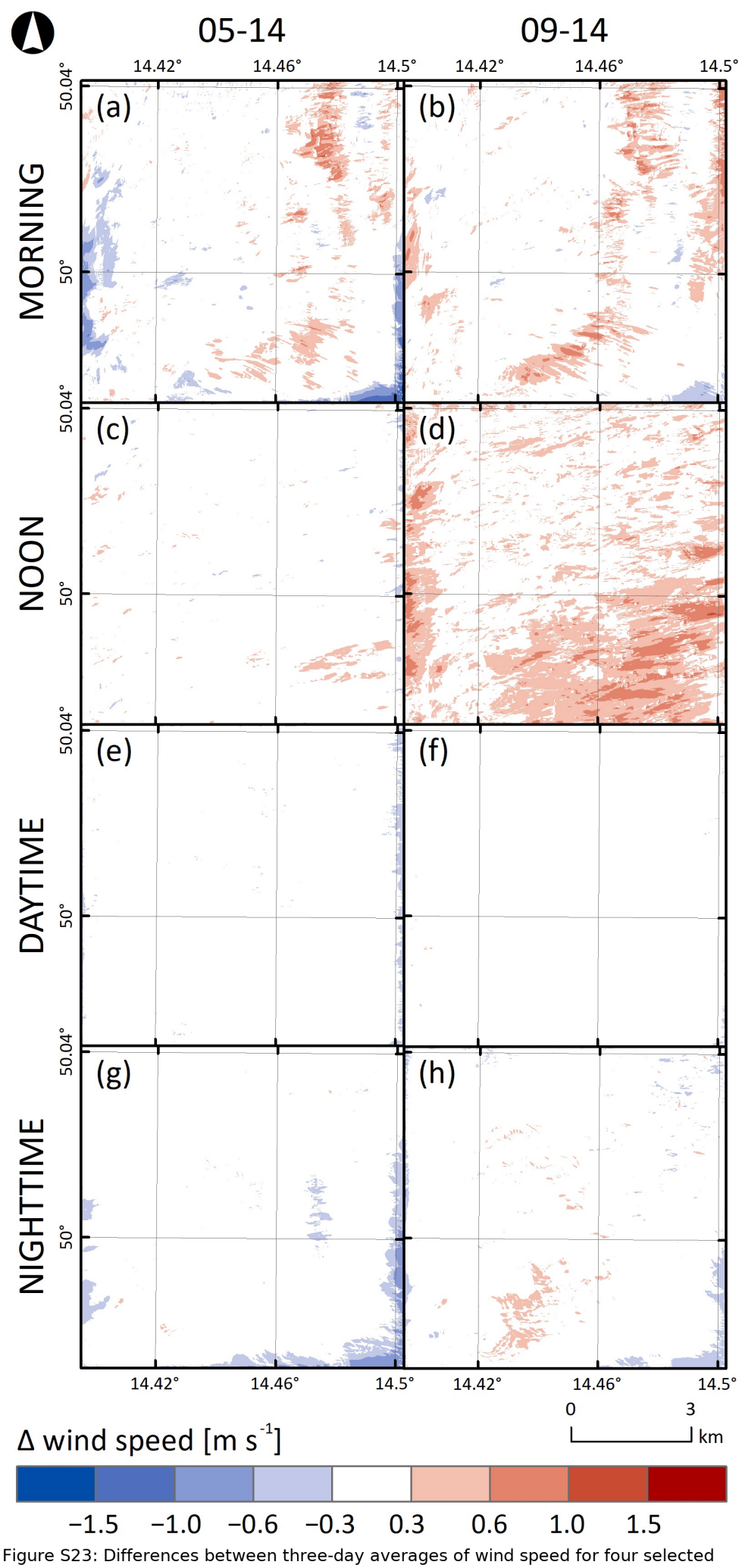

Figure S23: Differences between three-day averages of wind speed for four selected time periods (morning, noon, daytime, and nighttime) taken from the PALM model members 05, 09, and 14 for the e2 episode. The first column refers to the difference between 05 and 14 PALM model outputs (driven by the best and the worst WRF model members selected based on the potential temperature, respectively), the second column refers to the difference between 09 and 14 PALM model outputs (driven by the best and the worst WRF model members selected based on the wind speed, respectively).

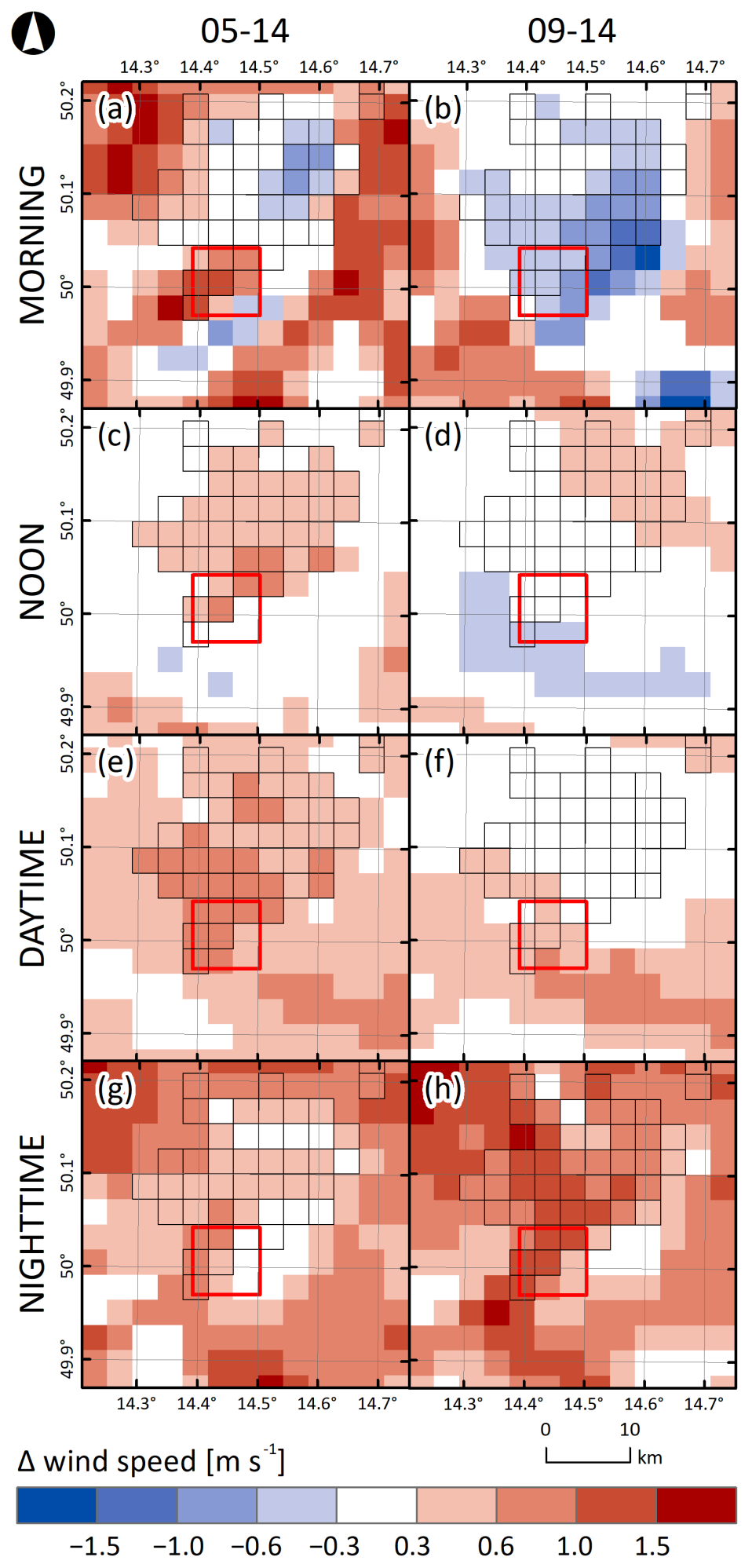

Figure S24: Differences between three-day averages of wind speed for four selected time periods (morning, noon, daytime, and nighttime) taken from the WRF model members 05, 09, and 14 for the e2 episode. The first column refers to the difference between the best (05) and the worst (14) WRF model members selected based on the potential temperature, the second column refers to the difference between the best (09) and the worst (14) WRF model members selected based on the wind speed. The PALM model simulation domain is depicted with the red square. The WRF model grid boxes in which the majority of landuse is of urban type are outlined with black color.

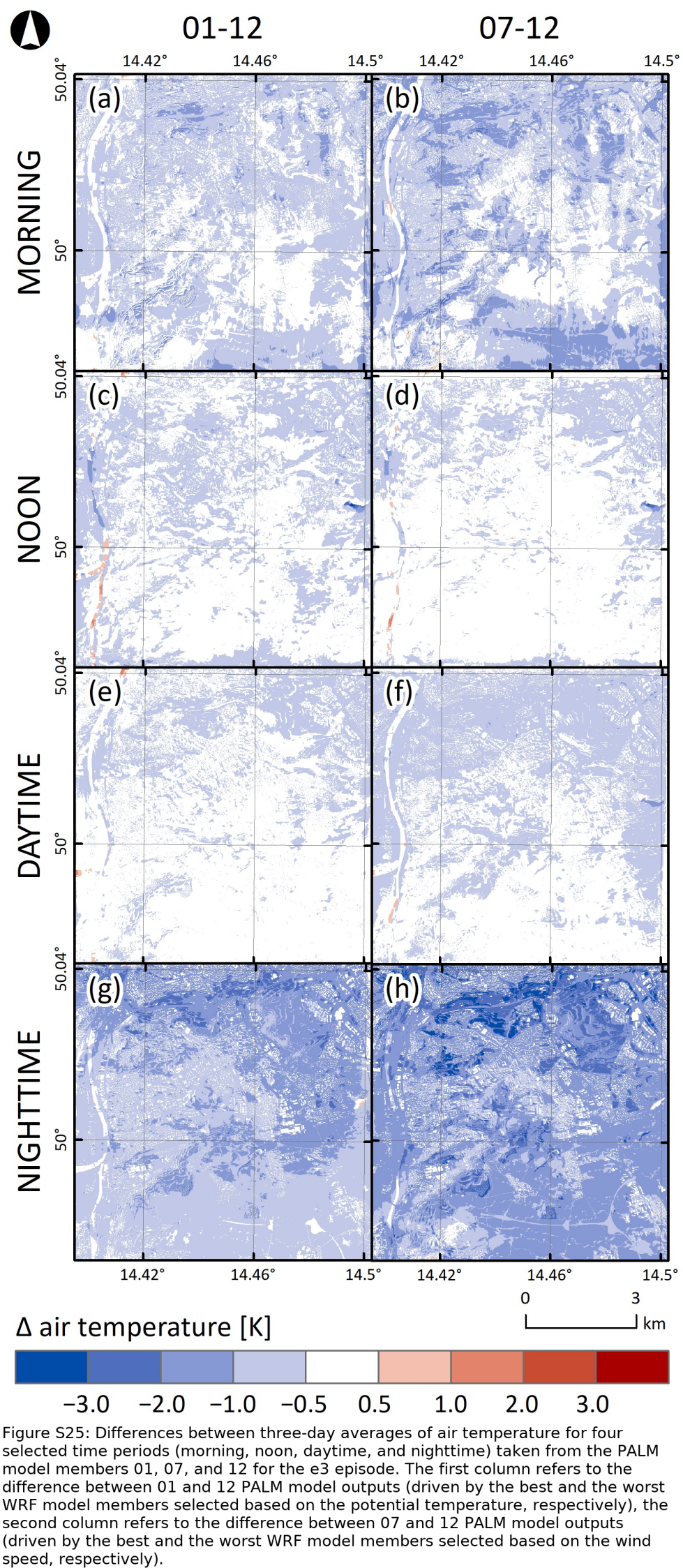

Figure S25: Differences between three-day averages of air temperature for four selected time periods (morning, noon, daytime, and nighttime) taken from the PALM model members 01, 07, and 12 for the e3 episode. The first column refers to the difference between 01 and 12 PALM model outputs (driven by the best and the worst WRF model members selected based on the potential temperature, respectively), the second column refers to the difference between 07 and 12 PALM model outputs (driven by the best and the worst WRF model members selected based on the wind speed, respectively).

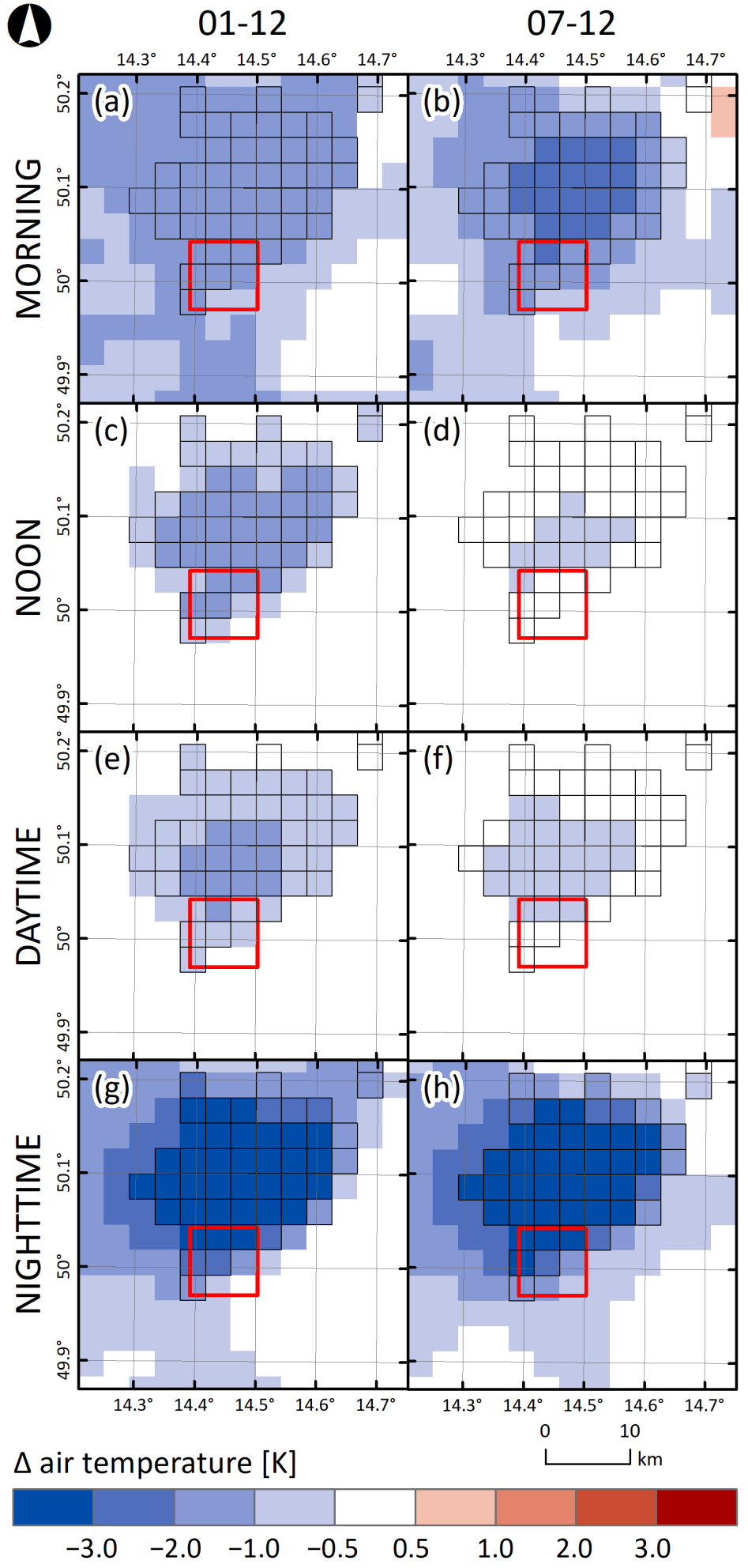

Figure S26: Differences between three-day averages of air temperature for four selected time periods (morning, noon, daytime, and nighttime) taken from the WRF model members 01, 07, and 12 for the e3 episode. The first column refers to the difference between the best (01) and the worst (12) WRF model members selected based on the potential temperature, the second column refers to the difference between the best (07) and the worst (12) WRF model members selected based on the wind speed. The PALM model simulation domain is depicted with the red square. The WRF model grid boxes in which the majority of landuse is of urban type are outlined with black color.

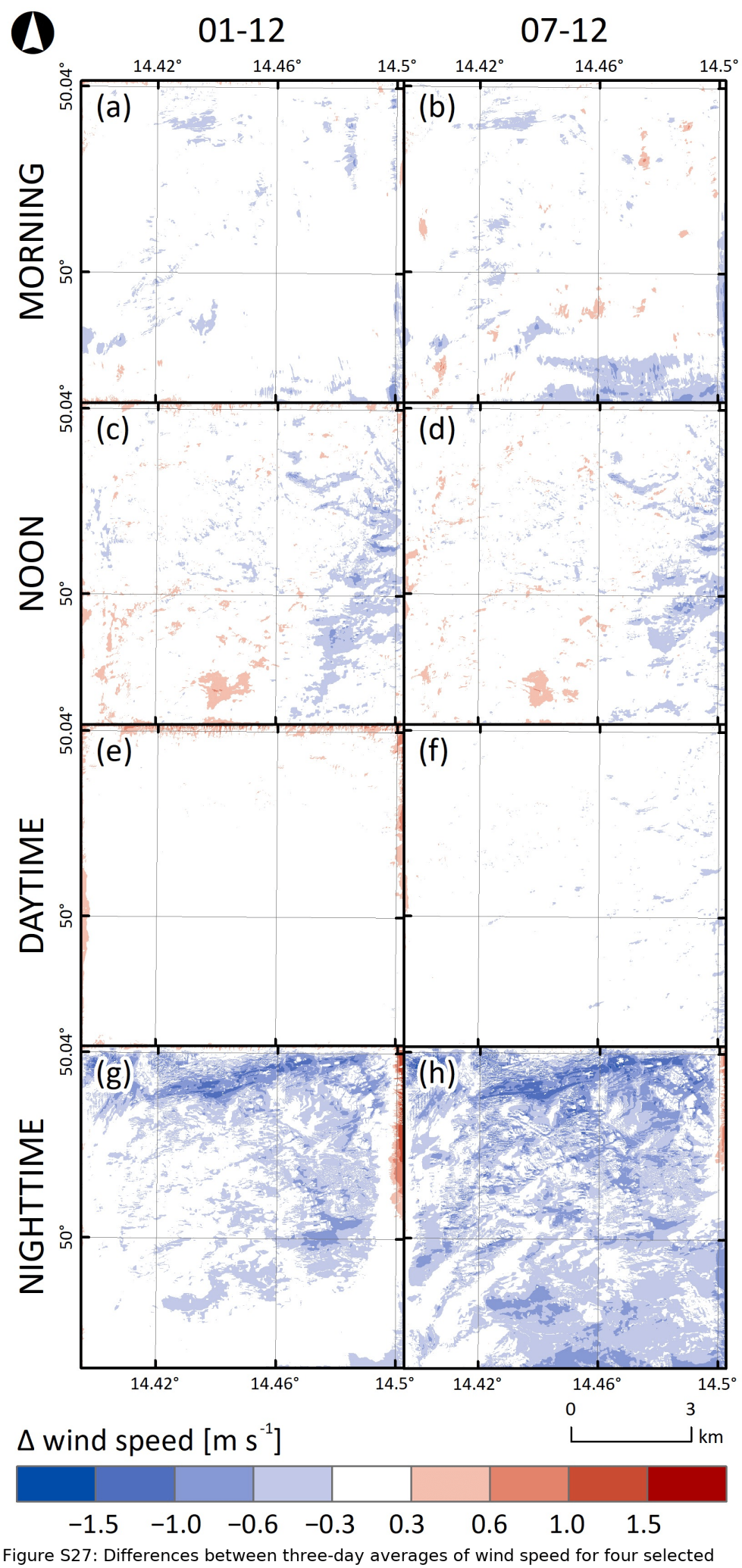

Figure S27: Differences between three-day averages of wind speed for four selected time periods (morning, noon, daytime, and nighttime) taken from the PALM model members 01, 07, and 12 for the e3 episode. The first column refers to the difference between 01 and 12 PALM model outputs (driven by the best and the worst WRF model members selected based on the potential temperature, respectively), the second column refers to the difference between 07 and 12 PALM model outputs (driven by the best and the worst WRF model members selected based on the wind speed, respectively).

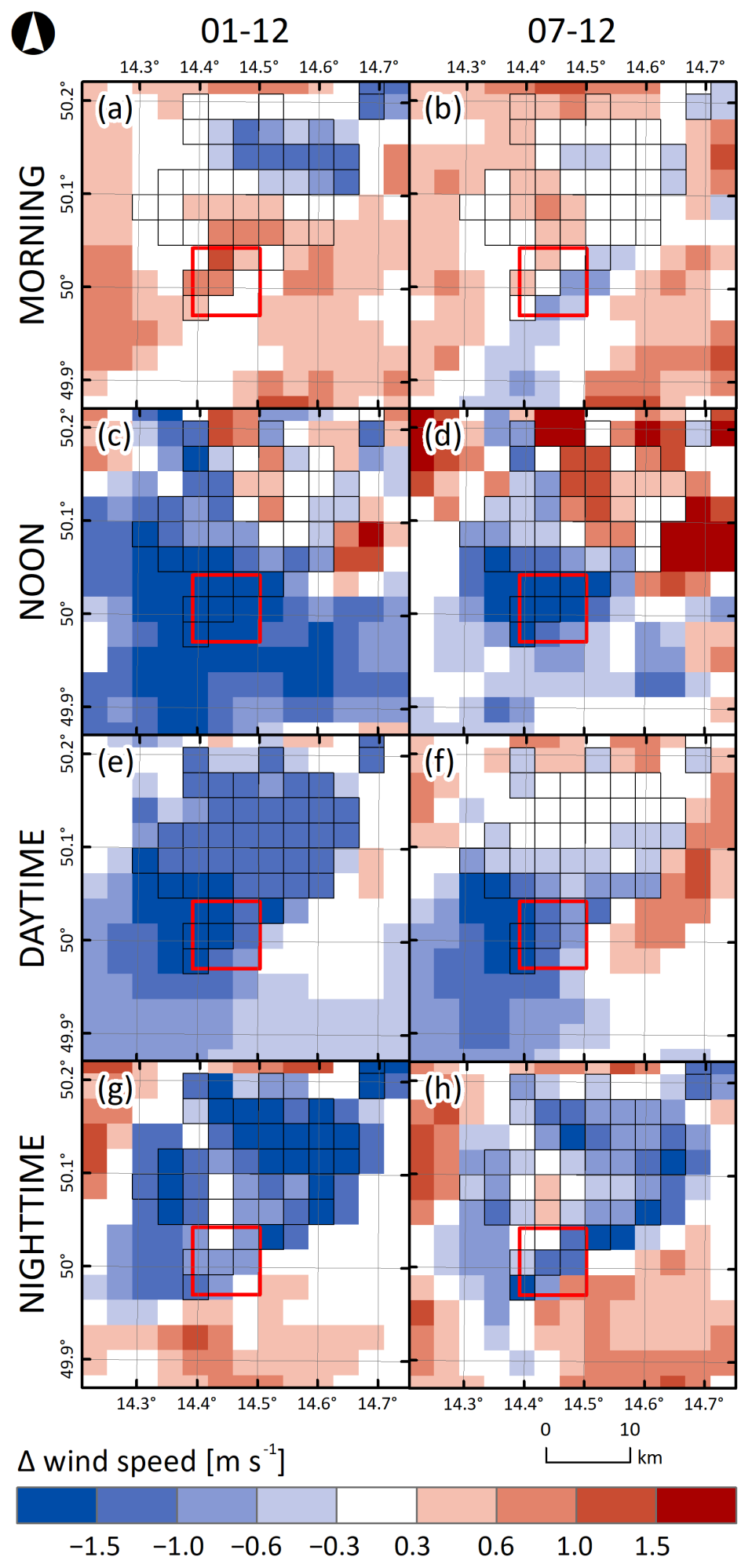

Figure S28: Differences between three-day averages of wind speed for four selected time periods (morning, noon, daytime, and nighttime) taken from the WRF model members 01, 07, and 12 for the e3 episode. The first column refers to the difference between the best (01) and the worst (12) WRF model members selected based on the potential temperature, the second column refers to the difference between the best (07) and the worst (12) WRF model members selected based on the wind speed. The PALM model simulation domain is depicted with the red square. The WRF model grid boxes in which the majority of landuse is of urban type are outlined with black color.

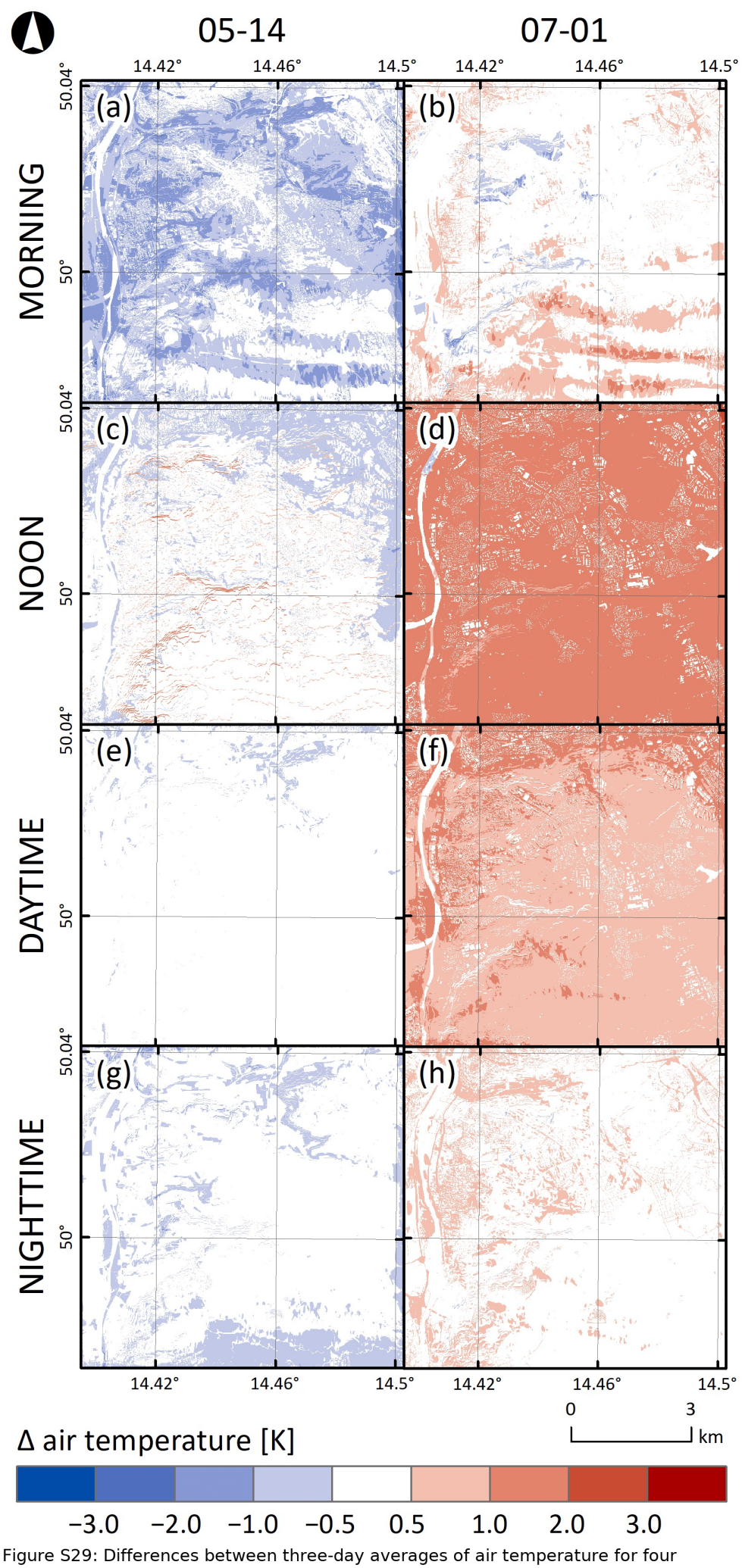

Figure S29: Differences between three-day averages of air temperature for four selected time periods (morning, noon, daytime, and nighttime) taken from the PALM model members 01, 05, 07, and 14 for the e4 episode. The first column refers to the difference between 05 and 14 PALM model outputs (driven by the best and the worst WRF model members selected based on the potential temperature, respectively), the second column refers to the difference between 07 and 01 PALM model outputs (driven by the best and the worst WRF model members selected based on the wind speed, respectively).

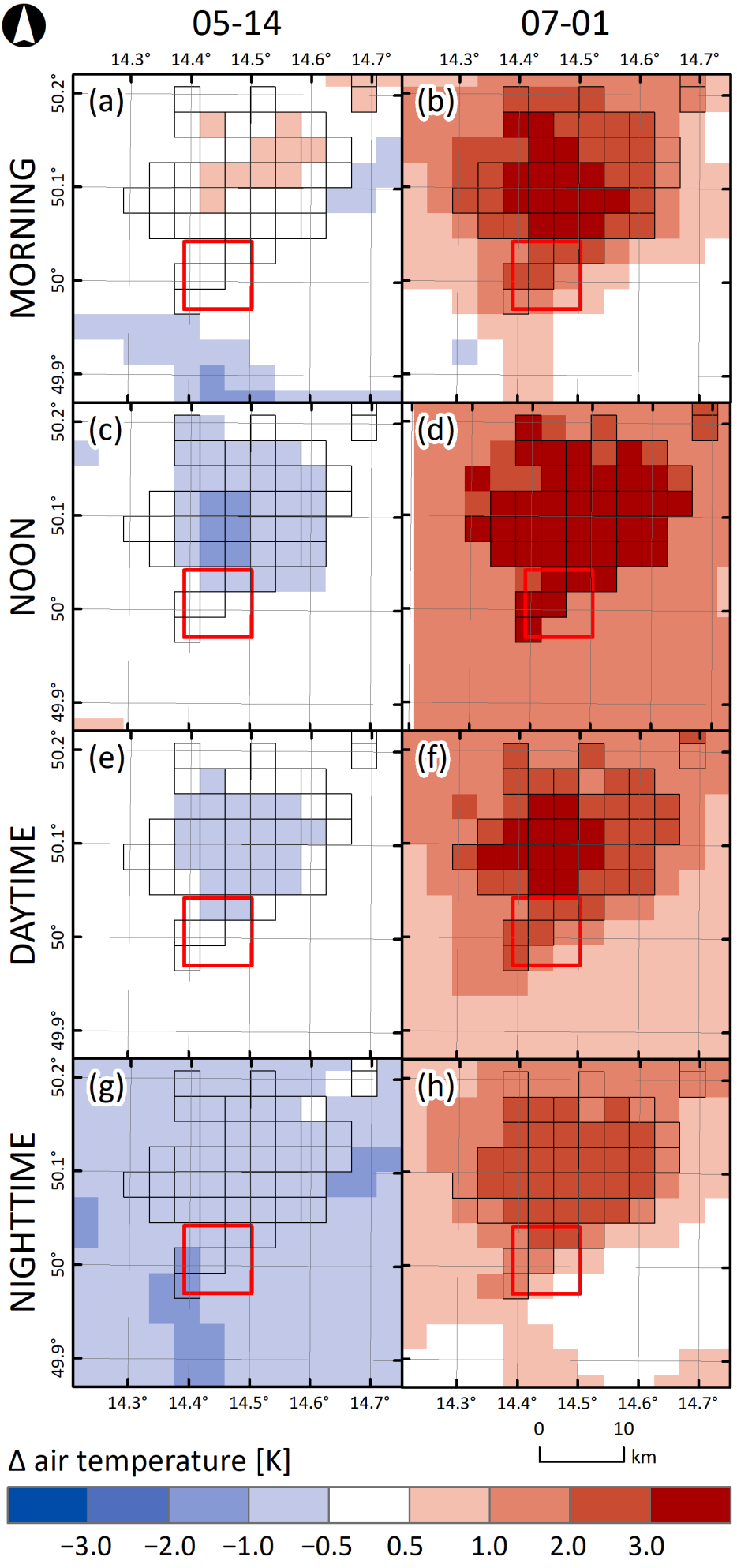

Figure S30: Differences between three-day averages of air temperature for four selected time periods (morning, noon, daytime, and nighttime) taken from the WRF model members 01, 05, 07, and 14 for the e4 episode. The first column refers to the difference between the best (05) and the worst (14) WRF model members selected based on the potential temperature, the second column refers to the difference between the best (07) and the worst (01) WRF model members selected based on the wind speed. The PALM model simulation domain is depicted with the red square. The WRF model grid boxes in which the majority of landuse is of urban type are outlined with black color.

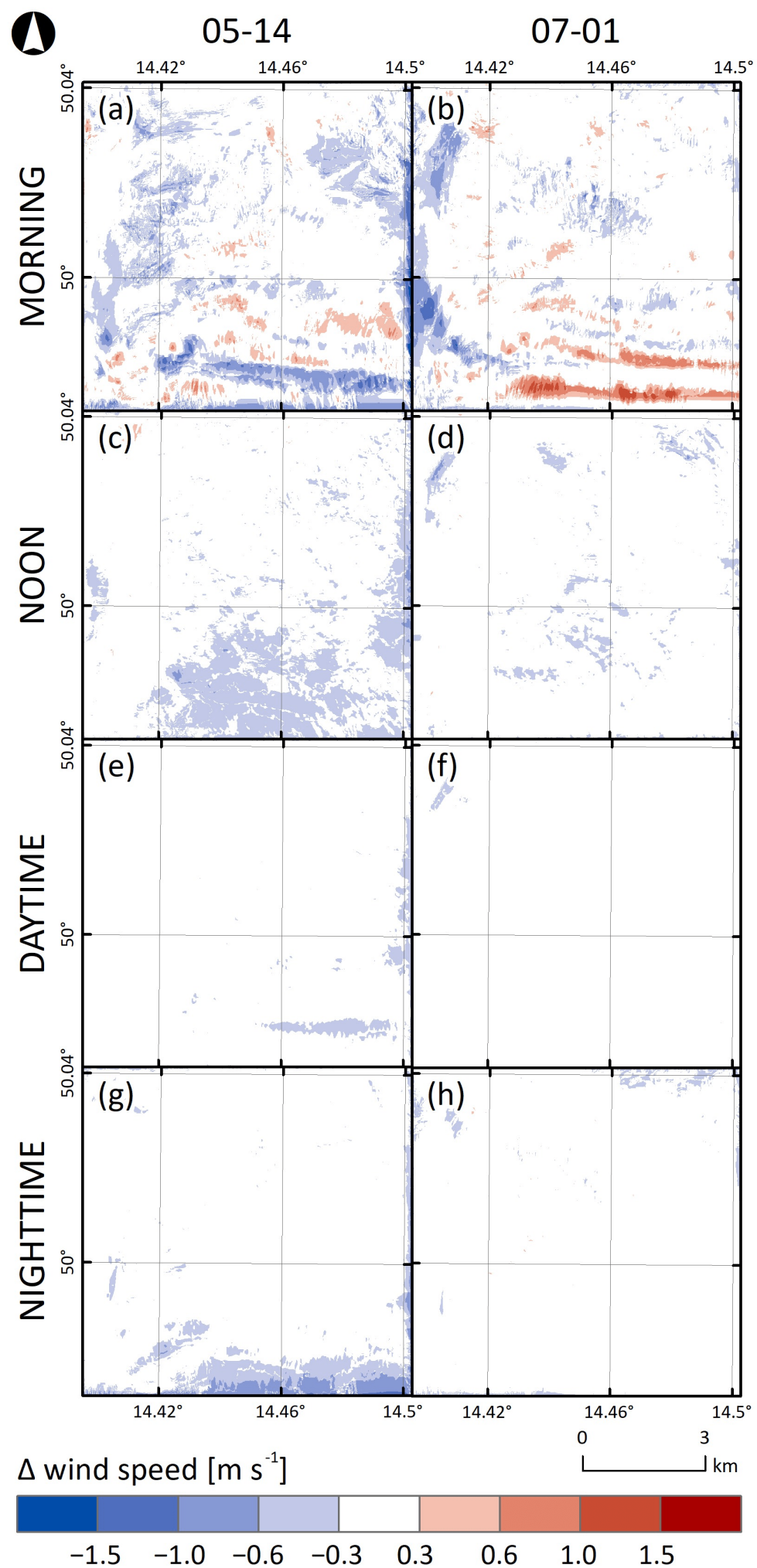

Figure S31: Differences between three-day averages of wind speed for four selected time periods (morning, noon, daytime, and nighttime) taken from the PALM model members 01, 05, 07, and 14 for the e4 episode. The first column refers to the difference between 05 and 14 PALM model outputs (driven by the best and the worst WRF model members selected based on the potential temperature, respectively), the second column refers to the difference between 07 and 01 PALM model outputs (driven by the best and the worst WRF model members selected based on the wind speed, respectively).

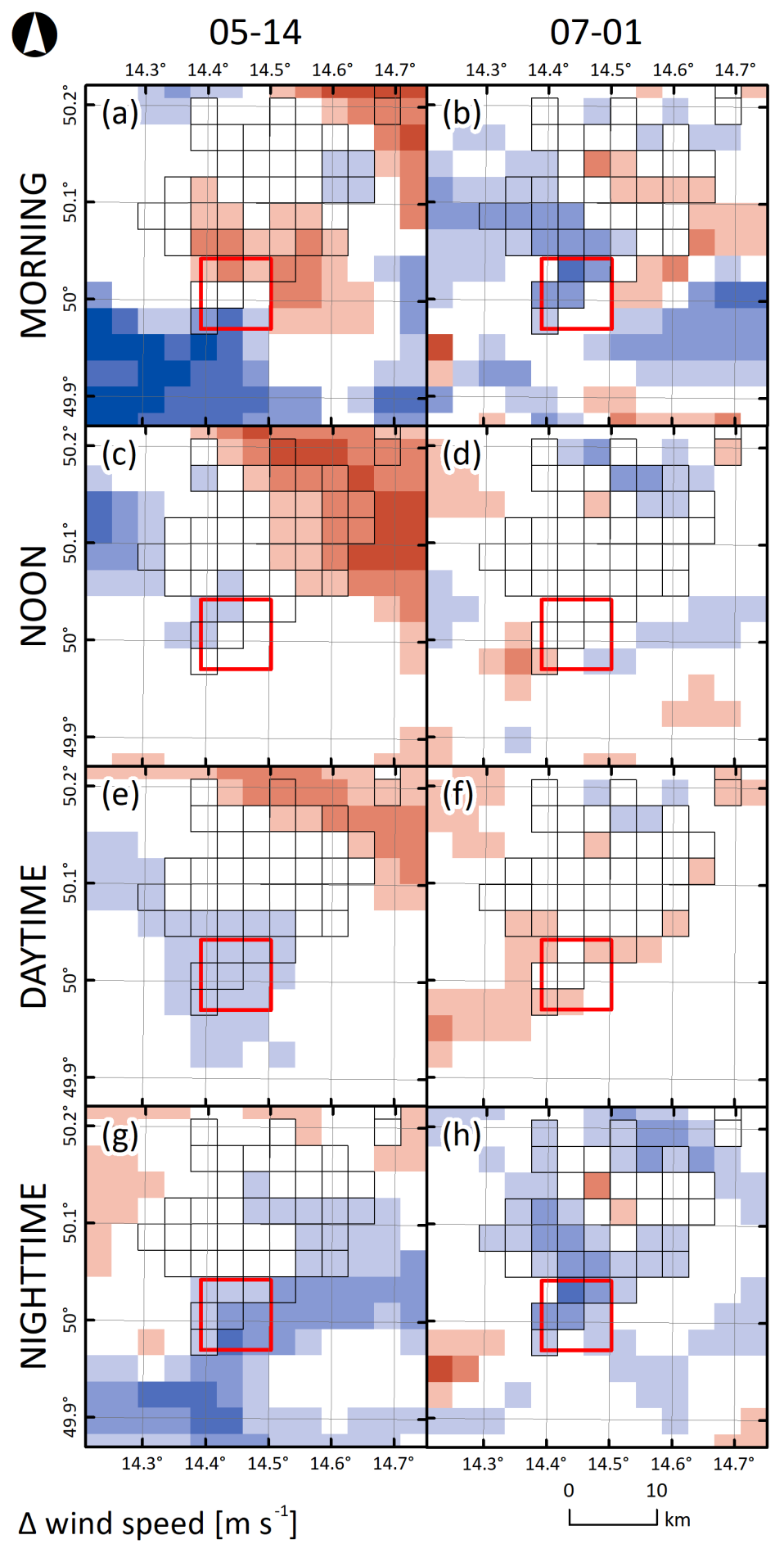

Figure S32: Differences between three-day averages of wind speed for four selected time periods (morning, noon, daytime, and nighttime) taken from the WRF model members 01, 05, 07, and 14 for the e4 episode. The first column refers to the difference between the best (05) and the worst (14) WRF model members selected based on the potential temperature, the second column refers to the difference between the best (07) and the worst (01) WRF model members selected based on the wind speed. The PALM model simulation domain is depicted with the red square. The WRF model grid boxes in which the majority of landuse is of urban type are outlined with black color.

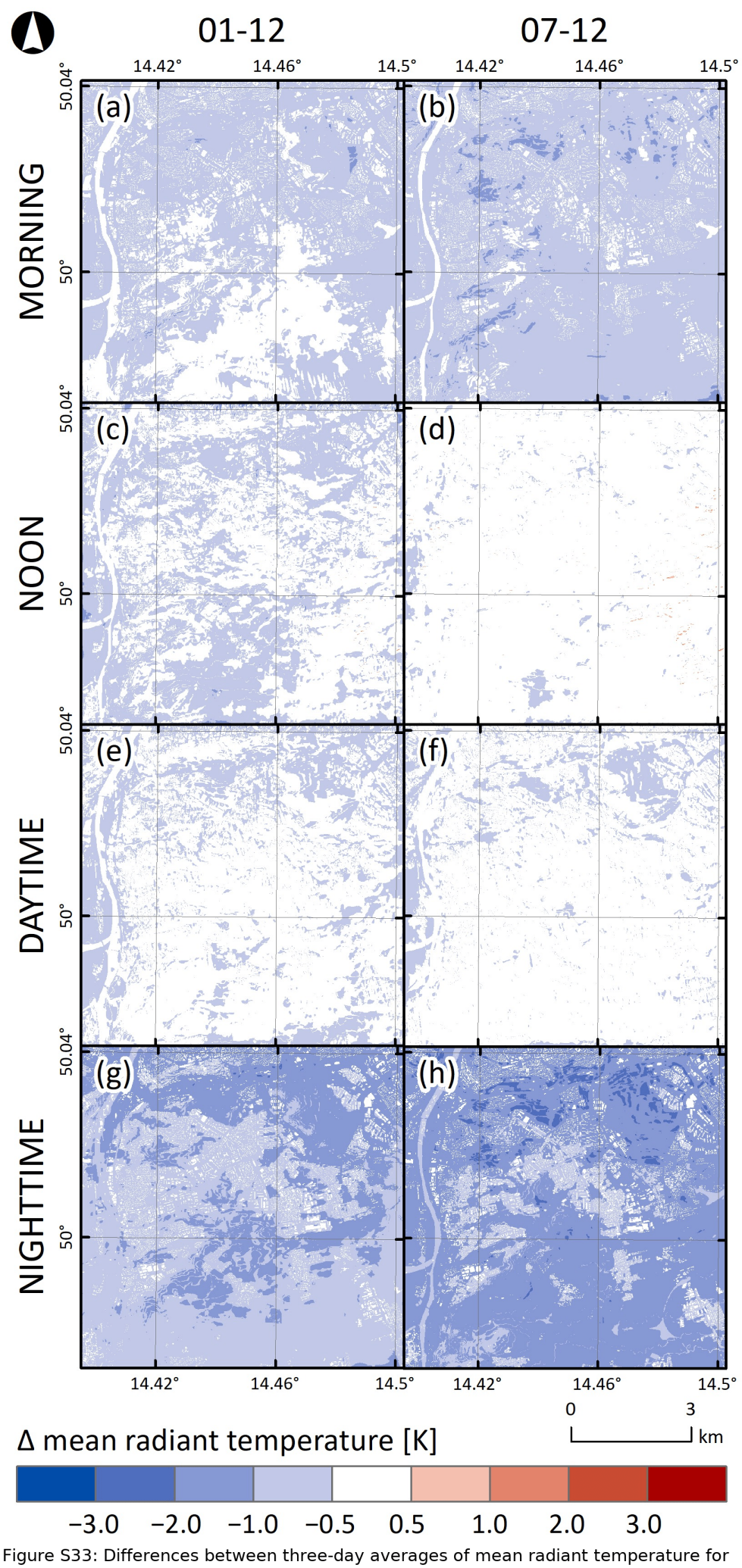

Figure S33: Differences between three-day averages of mean radiant temperature for four selected time periods (morning, noon, daytime, and nighttime) taken from the PALM model members 01, 07, and 12 for the e3 episode. The first column refers to the difference between 05 and 14 PALM model outputs (driven by the best and the worst WRF model members selected based on the potential temperature, respectively), the second column refers to the difference between 07 and 01 PALM model outputs (driven by the best and the worst WRF model members selected based on the wind speed, respectively).

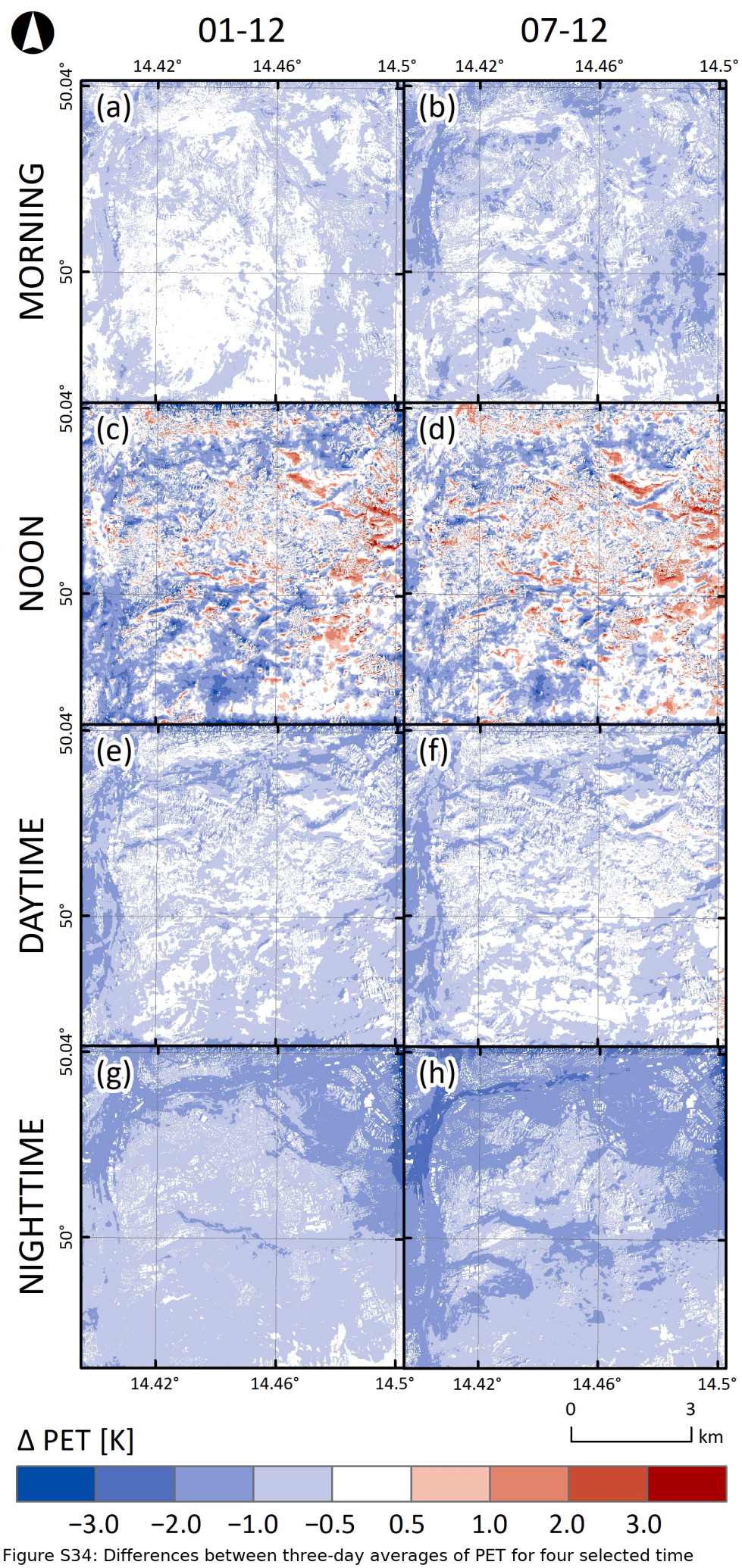

Figure S34: Differences between three-day averages of PET for four selected time periods (morning, noon, daytime, and nighttime) taken from the PALM model members 01, 07, and 12 for the e3 episode. The first column refers to the difference between 05 and 14 PALM model outputs (driven by the best and the worst WRF model members selected based on the potential temperature, respectively), the second column refers to the difference between 07 and 01 PALM model outputs (driven by the best and the worst WRF model members selected based on the wind speed, respectively).

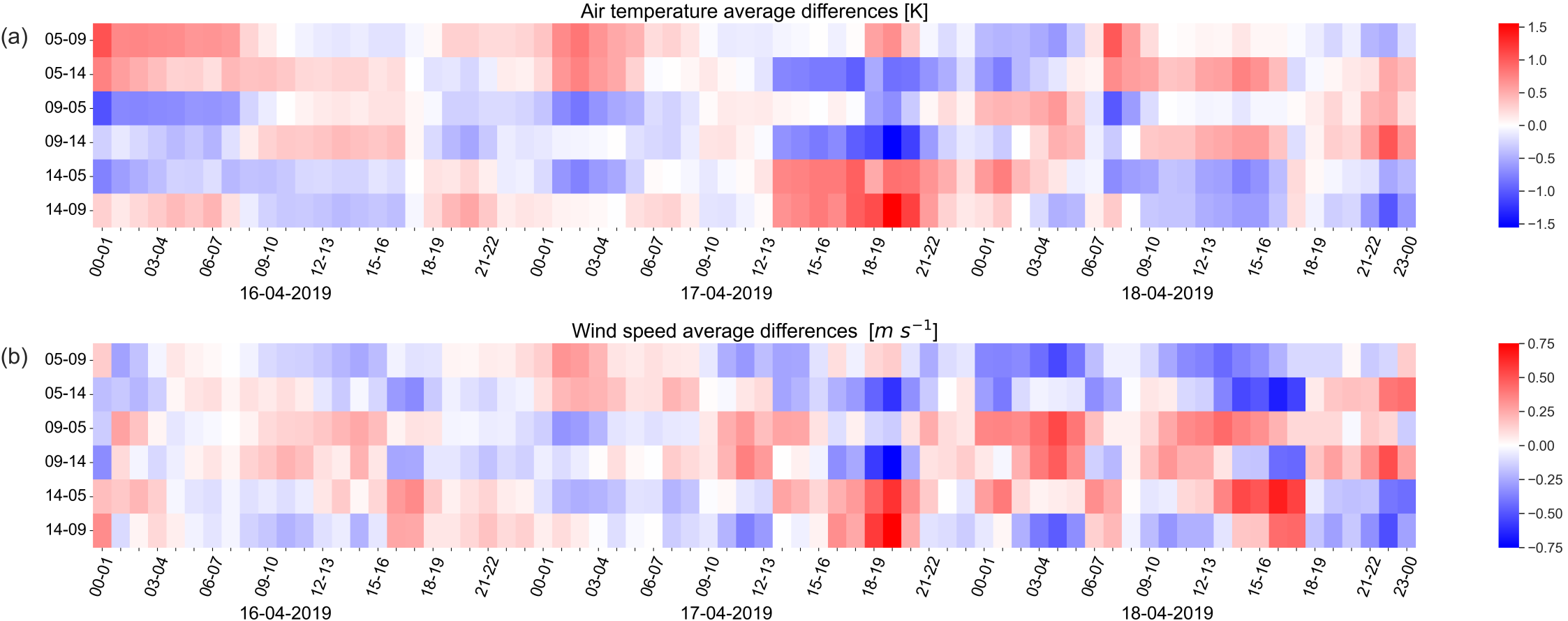

Figure S35: Spatially averaged 1hr average differences of air temperature (a) and wind speed (b) calculated for all the combinations taken from the PALM model outputs for the e2 episode. On the x-axis, the averaging hours in UTC along with the simulation dates are presented, and on the y-axis are the ID numbers of PALM model differences.

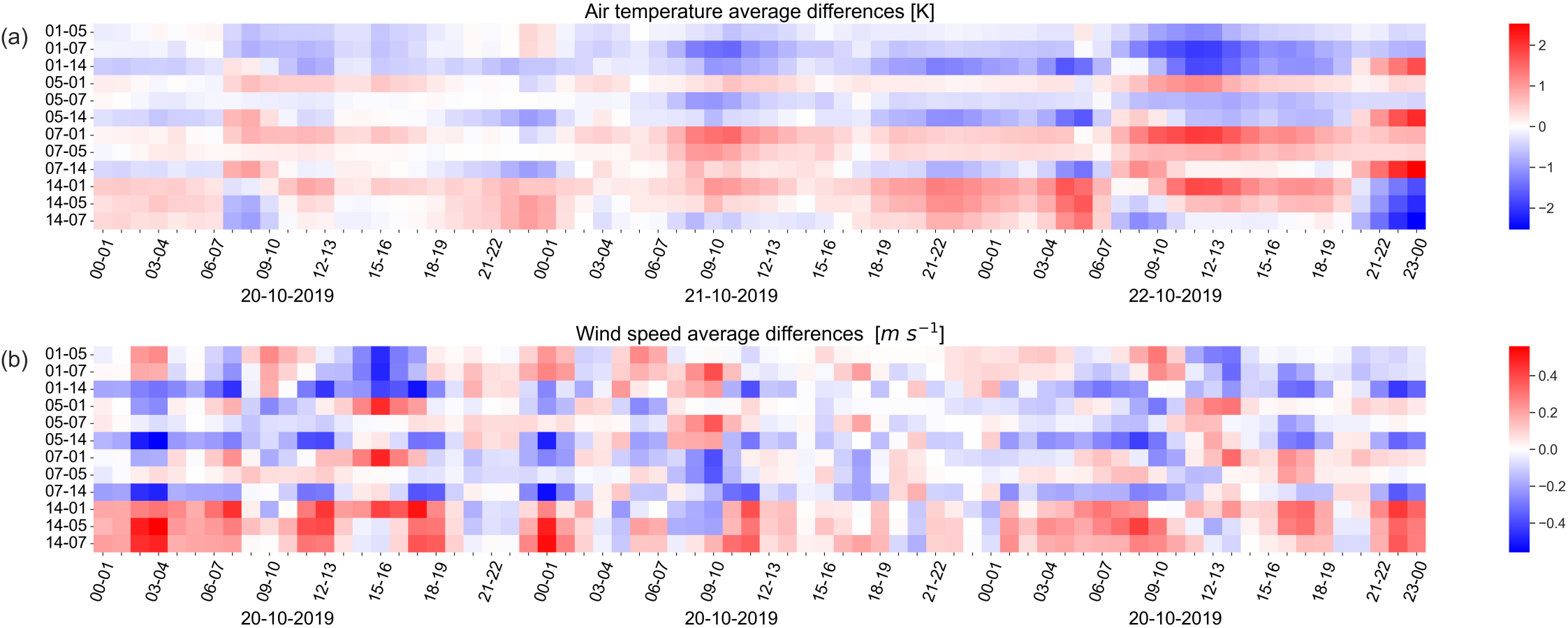

Figure S36: Spatially averaged 1hr average differences of air temperature (a) and wind speed (b) calculated for all the combinations taken from the PALM model outputs for the e4 episode. On the x-axis, the averaging hours in UTC along with the simulation dates are presented, and on the y-axis are the ID numbers of PALM model differences.

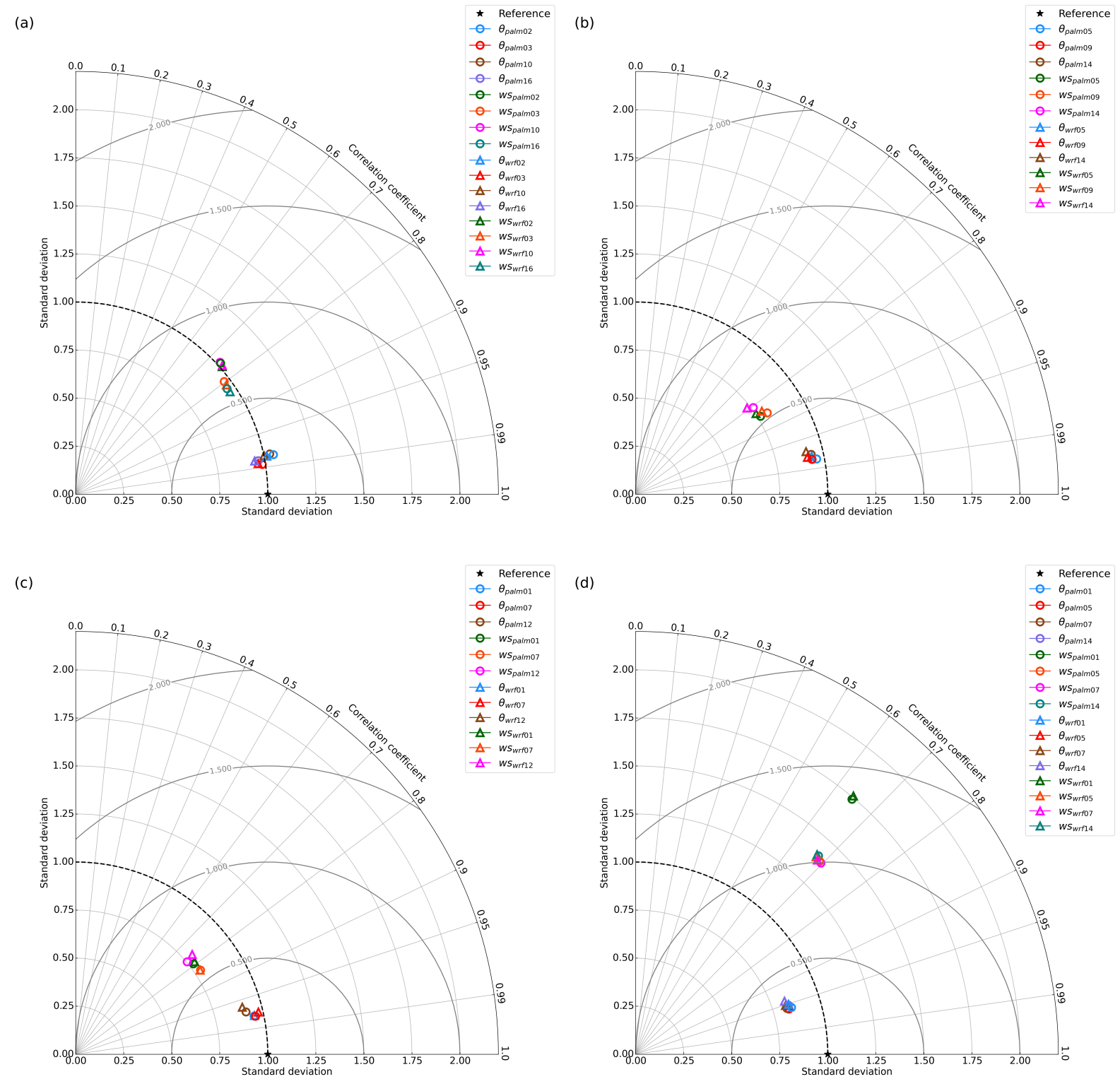

Figure S37: Normalized Taylor diagrams for February (a), April (b), July (c), and October (d) episodes calculated for vertical profiles of potential temperatures and wind speeds for the full height of 3000 m a.s.l. for each of the selected members for each of the episodes. The shapes of the points distinguish between the models: PALM-circle and WRF-triangle.The colors connect the same PALM and WRF memebrs for the specific episode.